Mechanically Versatile Soft Machines through Laminar Jamming

DOI: 10.1002/adfm.201707136
Article type: Full Paper

Mechanically Versatile Soft Machines Through Laminar Jamming

*Yashraj S. Narang, Joost J. Vlassak, Robert D. Howe**

Y. S. Narang, Prof. J. J. Vlassak, Prof. R. D. Howe
Paulson School of Engineering and Applied Sciences, Harvard University, Cambridge, MA 02138, USA
E-mail: howe@seas.harvard.edu

Keywords: laminar jamming, soft robotics, variable impedance, shape locking, variable kinematics

There are two major structural paradigms in robotics: soft machines, which are conformable, durable, and safe for human interaction; and traditional rigid robots, which are fast, precise, and capable of applying high forces. Here, we bridge the paradigms by enabling soft machines to behave like traditional rigid robots on command. To do so, we exploit laminar jamming, a structural phenomenon in which a laminate of compliant strips becomes strongly coupled through friction when a pressure gradient is applied, causing dramatic changes in mechanical properties. We develop rigorous analytical and finite element models of laminar jamming, and we experimentally characterize jamming structures to show that the models are highly accurate. We then integrate jamming structures into soft machines to enable them to selectively exhibit the stiffness, damping, and kinematics of traditional rigid robots. The models allow jamming structures to be efficiently designed to meet arbitrary performance specifications, and the physical demonstrations illustrate how to construct systems that can behave like either soft machines or traditional rigid robots at will, such as continuum manipulators that can rapidly have joints appear and disappear. Our study aims to foster a new generation of mechanically versatile machines and structures that cannot simply be classified as “soft” or “rigid.”

1. Introduction

Soft machines and traditional rigid robots have distinct forms and functions. Soft machines (e.g., elastomeric bending actuators[1,2] and dielectric elastomer grippers[3,4]) are made of compliant materials and bend or twist continuously along their length. Their actuation mechanism is typically distributed throughout their volume. Traditional rigid robots (e.g., robotic arms and humanoids) are made of stiff materials and bend or translate discretely at joints. Their actuation mechanism is usually confined to these joints. The structure of soft machines allows them to conform to complex shapes,[5,6] withstand crushing loads,[7] dampen impacts, and interact safely with the body.[8,9] In contrast, the structure of traditional rigid robots enables them to perform tasks quickly, precisely, and with high resolution, as well as resist deformation, apply high forces, and oscillate with minimal decay.

To make more versatile robots, researchers have aimed to enable soft machines to selectively behave like traditional rigid robots. In particular, soft machines have been constructed with materials and structures that can exhibit tunable stiffness and damping in order to attain the mechanical properties of traditional robots. These components include low-melting-point materials,[10,11] shape-memory materials,[12,13] magnetorheological (MR) fluids,[14] and granular structures.[9,15] Nevertheless, most of these technologies cannot achieve a wide range of stiffness and damping values per unit weight (MR fluids, granular structures), have low resolution of stiffness and damping values (low-melting-point materials), transition between these values slowly (low-melting-point materials, shape-memory materials), and/or have poor resistance to bending moments (MR fluids, granular structures).[9,16] Furthermore, none of these technologies have yet enabled devices to rapidly transition between the continuous deformations typical of soft machines and the discrete, jointed deformations typical of traditional robots. Previous efforts towards this goal have been limited by slow transition times, high stiffnesses when no power is applied, and low efficiencies.[10,17]

The laminar jamming (a.k.a., "layer jamming") phenomenon is a promising alternative to these technologies **(Figure 1A-B)**. Laminar jamming structures are lightweight and can be rapidly actuated; moreover, they can achieve excellent range and resolution of stiffness and damping values with high resistance to bending moments. A laminar jamming structure consists of a laminate of flexible strips or sheets. In its default state, the laminate is highly compliant. However, when a pressure gradient is applied (in this study, by enclosing the laminate in an airtight envelope and applying a vacuum to the envelope), increased frictional interactions dramatically augment the bending stiffness of the structure; in addition, at high loads, the structure dissipates energy. Researchers have applied laminar jamming to haptics,[18-20] medical devices,[21,22] and soft actuators.[23,24] Nevertheless, these studies have not yet provided analytical or computational models for laminar jamming beyond an initial deformation phase, making design of practical jamming structures an arduous process. Furthermore, they have not yet explored how laminar jamming can be used to transform bending kinematics.

In this paper, we model laminar jamming in detail and demonstrate how the technology can bridge the gap between soft machines and traditional rigid robots. Specifically, we develop an analytical model that mathematically captures how two-layer jamming structures behave over all major phases of deformation. We then develop finite element models that extend these predictions to many-layer jamming structures, as well as describe how their stiffness and damping depend on critical design inputs (e.g., the vacuum pressure). These models are validated through rigorous experimental characterization. Together, the analytical and finite element models present researchers with the first means to rapidly and accurately design jamming structures to meet arbitrary design requirements.

We then demonstrate the capabilities of laminar jamming structures by integrating them into real-world pneumatic and cable-driven soft machines. In the process, we achieve two novel functions that illustrate how these machines can reversibly emulate traditional rigid

robots: 1) *shape-locking*, in which a compliant system can selectively manifest a stiff version of a desired shape and preserve it, even after powering off the actuators, and 2) *variable kinematics*, in which a compliant system can transition between continuous bending and discrete, jointed bending on command. The variable kinematics function is then used to build a two-fingered grasper that can perform pinch grasps on small objects, as well as wrap grasps on objects of eight times the diameter. These demonstrations prove the feasibility of using laminar jamming to build mechanically versatile machines and structures that exhibit both soft and traditional behavior.

2. Results

2.1. Analytical Modeling

As described earlier, when a vacuum is applied to a laminar jamming structure, the bending stiffness increases dramatically. Previous studies have shown that the stiffness increases by a factor of $\boldsymbol{n^2}$, where $\boldsymbol{n}$ is the number of layers in the structure; thus, applying a vacuum to a structure with just thirty-two layers can increase its stiffness by three orders of magnitude. However, the vacuumed jamming structure sustains this increased stiffness only over a limited range of loads, beyond which the stiffness declines.[18,21]

In our investigation, physical reasoning suggested that this behavior reflected three phases of deformation in a vacuumed jamming structure **(Figure 1C-D)**: 1) In *pre-slip*, the layers are cohesive, and the stiffness of the structure is a factor of $\boldsymbol{n^2}$ greater than the stiffness without vacuum. No energy is dissipated, and the damping (i.e., dissipated energy per unit deflection) is zero. As the structure is loaded, the longitudinal shear stress along the interfaces between layers begins to rise. 2) In the *transition regime*, the longitudinal shear stress along certain regions of the interfaces equals the maximum possible shear stress, which is determined by the coefficient of friction and the pressure gradient. Layers begin to slip along

those regions, and the stiffness of the structure decreases. Energy is dissipated to friction, and the damping increases. 3) In *full-slip*, all layers have slipped along the full length of their interfaces. The stiffness of the structure is minimal, and the damping is maximal.

To mathematically capture this behavior, we derived an analytical model that rigorously described the deformation and mechanical properties of jamming structures during these phases. Our model was based on Euler-Bernoulli beam theory; however, we extended the theory to describe how mechanical behavior was affected by vacuum pressure, friction at the interfaces between layers, and slip along the interfaces. Governing equations were derived using equilibrium and moment-stress relations, and general boundary conditions were formulated **(SI: Analytical Modeling: Governing Equations** and **Boundary Conditions)**. The boundary-value problem was then solved for a two-layer cantilevered jamming structure under a uniform distributed load **(SI: Analytical Modeling: Explicit Solution)**; this case was chosen to illustrate slip propagation (i.e., growth of the regions along which layers slip), which is exhibited by most jamming structures.

The model predicted the elastica (i.e., the shape), stiffness, dissipated energy, and damping of the jamming structure. The model also predicted the transition loads (i.e., the loads at which the jamming structure shifts from one deformation phase to the next), as well as the length of the region along which the layers slipped. Furthermore, it provided the functional dependence of all the preceding quantities on dimensions, material properties, the vacuum pressure, and the applied load **(SI: Analytical Modeling: Summary of Formulae)**. For example, the model showed that the full-slip damping force was given succinctly by $\boldsymbol{\mu P b h}$, where $\boldsymbol{\mu}$ is the coefficient of friction, $\boldsymbol{P}$ is the vacuum pressure, $\boldsymbol{b}$ is the width of a layer, and $\boldsymbol{h}$ is the height. Dimensionless forms of the equations in the model were derived as well (**SI: Analytical Modeling: Dimensionless Forms)**. The model was evaluated for an

example structure **(Figure 2)**, and the results were corroborated by two-layer finite element models **(SI: Finite Element Modeling: Two-Layer Jamming Structures)**.

2.2. Finite Element Modeling and Experimental Characterization

Although the analytical model rigorously predicted the mechanical behavior of two-layer jamming structures, designers may desire to build real-world jamming structures with additional layers to further adjust their properties. Our analytical model can be directly extended to describe many-layer jamming structures **(SI: Analytical Modeling: Extending the Model)**. However, the process is algebraically taxing, and numerical methods may be preferred.

To predict the mechanical behavior of many-layer jamming structures, we conducted finite element simulations. The jamming structures were modeled as 2D plane-strain structures with dimensions, material properties, boundary conditions, and loads equal to those of real-world jamming structures used later in experimental validation **(SI: Finite Element Modeling: Stiffness** and **Damping of Many-Layer Jamming Structures)**. Furthermore, simultaneous frictional contact was allowed to occur at all interfaces, and large-deformation analysis was enabled. No fitting parameters were used.

The results of the finite element simulations were used to quantify how critical design inputs affected major performance metrics of many-layer jamming structures. Specifically, the number of layers, vacuum pressure, and coefficient of friction of the layers were varied, and the stiffness and damping values of the jamming structures during pre-slip and full-slip were extracted. The polynomial relationship between each input and output was determined, and the resulting scaling relations were tabulated **(SI: Finite Element Modeling: Functional Dependencies)**. For example, full-slip damping was found to scale linearly with number of layers, vacuum pressure, and coefficient of friction.

To evaluate the accuracy of the finite element models, experimental characterization of many-layer jamming structures was conducted. Jamming structures were fabricated according to a multi-step process **(SI: Experimental Characterization: Fabrication Process)**, and the repeatability of the structures was assessed **(SI: Experimental Characterization: Repeatability Analysis)**. The jamming structures were highly repeatable from loading cycle to loading cycle and sample to sample. The many-layer jamming structures were then tested in three-point bending for various numbers of layers and vacuum pressures **(SI: Experimental Characterization: Stiffness** and **Damping Characterization Process)**. Transverse force and maximum deflection was recorded, and finite element predictions were compared to experimental data **(Figure 3)**. The finite element models predicted experimental results with exceptional accuracy.

2.3. Useful Functions

2.3.1. Shape-Locking

Two real-world capabilities of laminar jamming structures were demonstrated by integrating them into soft machines. First, the shape-locking function was demonstrated. A pneumatically powered soft bending actuator was fabricated **(SI: Functions and Applications: Shape-Locking)**, and a twenty-layer jamming structure was adhered to the ventral surface (i.e., the longitudinal surface closer to the center of curvature when the actuator was inflated). The actuator was then pressurized. When the actuator was depressurized, the system naturally returned to its undeformed configuration; however, when a vacuum was applied to the jamming structure before the actuator was depressurized, the system preserved its shape with high fidelity **(Figure 4)**.

2.3.2. Variable Kinematics

Next, the variable kinematics function was demonstrated. A robotic system was designed that consisted of three major parts: a silicone rubber substrate, a three-part jamming structure (i.e., three stacks of material, separated by narrow gaps), and a cable routed through the substrate to actuate bending **(Figure 5A)**. Note that when the rubber substrate and the vacuumed state of the jamming structure are considered separately, their bending kinematics are entirely distinct. The substrate bends continuously along its length, whereas the vacuumed jamming structure bends discretely at its narrow gaps, which act as joints. When the substrate and the jamming structure are adhered, the bending kinematics of the system may vary between these two extremes.

To enable the system to transition between continuous and discrete kinematics, the bending stiffnesses of the substrate and jamming structure were judiciously selected. The thickness of the substrate was chosen so that $\boldsymbol{k_{sub}} = \left(\boldsymbol{k_{jam}^{nv}} * \boldsymbol{k_{jam}^{v}}\right)^{\frac{1}{2}}$, where $\boldsymbol{k_{sub}}$ is the bending stiffness of the substrate, $\boldsymbol{k_{jam}^{nv}}$ is the stiffness of the jamming structure without vacuum, and $\boldsymbol{k_{jam}^{v}}$ is the pre-slip stiffness of the jamming structure with vacuum. (In equivalent terms, $\boldsymbol{k_{sub}}$ was the geometric mean of the unjammed and jammed stiffnesses.) In addition, the number of layers in the jamming structure was chosen so that $\boldsymbol{k_{jam}^{v}} >> \boldsymbol{k_{jam}^{nv}}$. Thus, when no vacuum was applied and the cable was pulled, the stiffness of the system would be dominated by $\boldsymbol{k_{sub}}$, and the system would bend continuously. When vacuum was applied, the stiffness would be dominated by $\boldsymbol{k_{jam}^{v}}$, and the system would bend discretely.

To evaluate this concept prior to prototyping, finite element simulations of the system were conducted **(SI: Finite Element Modeling: Variable Kinematics)**. The system was modeled as a multi-part 2D plain-strain structure fixed at one end, and to approximate cable loading, a pure moment load was applied at the free end. The shape of the system was visualized, and the ratio of maximum to mean curvature $\left(\frac{\boldsymbol{\kappa_{max}}}{\boldsymbol{\kappa_{mean}}}\right)$ was computed along the ventral arc as a measure of discreteness. When no vacuum was applied, the system deformed

continuously, and $\frac{\kappa_{max}}{\kappa_{mean}}$ remained low. When vacuum was applied, the system deformed discretely, and $\frac{\kappa_{max}}{\kappa_{mean}}$ increased by a factor of $\mathbf{6.65}$ at high loads **(Figure 5B-C)**.

Finally, a prototype of the system was fabricated **(SI: Functions and Applications: Variable Kinematics)**. The prototype deformed according to finite element predictions, and application of vacuum allowed it to select between continuous and discrete kinematics **(Figure 5D)**.

2.4. Application

2.4.1. Two-Fingered Grasper

In robotic hands, compliant fingers that bend continuously can facilitate wrap grasps around large objects,[25] whereas rigid fingers that bend discretely at joints can facilitate pinch grasps around smaller objects;[26,27] it is challenging to design and fabricate hands capable of both. To accomplish the task, we built a two-fingered grasper in which each finger consisted of a cable-actuated variable kinematics system with a rounded fingertip. When no vacuum was applied and the cables were pulled, the fingers bent continuously, and the device could perform a stable wrap grasp on a ball of diameter $\mathbf{20}\ \boldsymbol{cm}$. When vacuum was applied first, the fingers bent discretely, and the device could perform a stable pinch grasp on a ball of one-eighth the diameter **(Figure 5E)**.

To evaluate the stability of the grasps, multi-axis stiffness measurements were conducted and a perturbation test was performed **(SI: Functions and Applications: Two-Fingered Grasper)**. Stiffness measurements showed that the maximum bending stiffness of a finger increased by at least a factor of thirty-two when vacuum was applied. Simultaneously, the off-axis bending stiffness (i.e., the stiffness along the perpendicular bending axis) increased by a factor of $\mathbf{2.5}$, and the torsional stiffness increased by a factor of $\mathbf{2.7}$.

Furthermore, perturbation tests demonstrated that the force required to dislodge the small ball was at least a factor of eight greater when vacuum was applied and the discretely-bending fingers were used, compared to when no vacuum was applied and the continuously-bending fingers were used. As an additional feature, applying vacuum after the continuously-bending fingers performed a grasp increased their resistance to further deformation.

3. Discussion

3.1. Modeling

Earlier studies of laminar jamming exclusively predicted the stiffness of jamming structures during pre-slip, as well as the first transition load (i.e., the load at which the structures move from pre-slip to the transition regime).[18,21,28] In contrast, our analytical model predicted the elastica, stiffness, energy dissipation, and damping of two-layer jamming structures during pre-slip, the transition regime, and full-slip, as well as determining both the first transition load and the second transition load (i.e., the load at which the structures move from the transition regime to full-slip). Our finite element models of many-layer jamming structures then extended the predictions of the analytical model to structures with arbitrary numbers of layers. Thus, the analytical and finite element models completely described the mechanical behavior of jamming structures over all three phases of deformation.

Together, the models provide designers with an accurate and efficient means to predict the mechanical behavior of arbitrary jamming structures. In particular, no models have existed for mechanical behavior in the transition regime or full-slip. To determine how a particular jamming structure will behave in these phases, designers have had to fabricate and characterize the structure. In our experience, this process requires hours of continuous labor per structure. In contrast, the analytical model can predict experimental behavior for a two-

layer jamming structure immediately, and a finite element simulation can predict experimental behavior for a many-layer structure in less than one hour without supervision.

In addition, the functional dependencies of performance metrics on design inputs were extracted for many-layer jamming structures. These relations provide researchers with a rapid means to meet arbitrary design requirements. For instance, if the full-slip stiffness of a jamming structure must be reduced by a factor of four (e.g., for an orthosis that softens at high loads for user safety), the relations show that the number of layers or vacuum pressure can be reduced by a factor of four, or the coefficient of friction can be reduced by a factor of two **(Table S1)**. Likewise, if the full-slip damping of a jamming structure must be increased by a factor of four (e.g., for a field robot that dampens impacts to protect components), then the number of layers, vacuum pressure, or coefficient of friction can be increased by a factor of four. The vacuum pressure can be controlled on command with a vacuum regulator; thus, full-slip stiffness and damping can be adjusted in real-time. The finite element models can be used to derive functional dependencies between additional performance metrics and design inputs as desired. Note that although the models and experiments in this study investigated jamming structures with a maximum of twenty layers, the extracted functional dependencies are applicable to structures with arbitrary numbers of layers; however, as the number of layers increases, it may become challenging to physically achieve a homogeneous vacuum pressure throughout the structure.

3.2. Useful Functions

Previous studies applied laminar jamming to diverse applications. However, these studies almost exclusively used laminar jamming to control stiffness; furthermore, when the jamming structures were integrated with actuators, the structures controlled the stiffness of the system while the actuators were continuously powered. We expanded on these capabilities by demonstrating shape-locking and variable kinematics. The former enables soft machines to

preserve their shape after the actuation input is removed, whereas the latter enables them to select between continuous and discrete bending.

Shape-locking illustrates one way in which laminar jamming structures can enable soft machines to reversibly emulate traditional rigid robots. Nearly all traditional robotic arms can navigate to an arbitrary location in their workspace and resist static loading. Furthermore, some arms have brakes that allow them to resist loading after power is disconnected. Shape-locking endows soft machines with precisely this ability, as it enables them to achieve an arbitrary configuration, lock in place, and resist static loading, even after disconnecting the actuation input. Soft machines can thus save power by requiring no control effort to preserve their shape; furthermore, soft machines with high material strain (e.g., McKibben actuators) can be deflated after locking, mitigating the risk of catastrophic rupture. Shape-locking may also be achieved by combining soft actuators with other materials and structures capable of tunable stiffness and damping, such as recently-developed thermally-activated fibers and composites;[29-31] however, laminar jamming offers a promising combination of rapid actuation, human safety, and high range of bending stiffness between the deforming and shape-locked states.

Variable kinematics comprises a second way in which laminar jamming structures can link the behavior of soft machines and traditional rigid robots. Specifically, this function can allow soft machines to rapidly transform between a highly compliant state in which they can conform to arbitrary shapes, and a rigid, jointed state in which they can behave like a serial manipulator. As demonstrated in this study, variable kinematics can enhance the performance of robotic graspers. Moreover, this capability can be useful for any device where both conformability and rigidity are desired (e.g., in surgical devices that must traverse vasculature, but subsequently apply high forces).

More generally, variable kinematics facilitates the modeling, sensing, and control of soft machines. For traditional rigid robots, multi-rigid-body mechanics can describe forward

and inverse kinematics; on the other hand, soft machines require the mathematical tools of continuum mechanics, which are generally far more complex. Furthermore, in traditional rigid robots, a small number of sensors can accurately estimate configuration; in soft machines, many sensors are required. Because modeling and sensing is more complex for soft machines, control is inherently more difficult.[32] Variable kinematics allows soft machines to behave like multi-rigid-body systems, with rigid links connected by joints. Thus, they can be modeled and sensed like traditional rigid robots, greatly simplifying their control. (It is interesting to note that octopuses use variable kinematics to simplify control, creating joints along their tentacles to facilitate fetching tasks.[33])

3.3. Limitations

Our modeling and demonstrations have three notable limitations, each of which can be resolved as described. First, in our finite element models of many-layer jamming structures, the execution time of the simulations scaled linearly with the number of layers; for models of jamming structures with exceptionally high numbers of layers, the time may become prohibitive. Nevertheless, as the numbers of layers increases in a jamming structure with a fixed total thickness, the structure may be accurately approximated as a single crystal with a single slip system. This structure can be simulated more simply than a multi-layer structure, reducing execution time **(SI: Finite Element Modeling: Limiting Behavior)**.

Second, in our shape-locking demonstration, our prototype still required a vacuum source to be connected after depressurization. Thus, the device would be challenging to operate in environments where supporting equipment is unavailable. This difficulty could be resolved by using a one-way valve to maintain vacuum after the vacuum input is disconnected.

Third, in our demonstrations, vacuum was used to actuate the jamming structures. As a result, the maximum pressure gradient acting on the jamming structures was limited to the

absolute ambient pressure, which in turn reduced the maximum load that could be sustained by the structures before their stiffness declined. This limit may be overcome by using electrostatic actuation[28] or elastic actuation, in which the layers are reversibly compressed by an external elastic structure (e.g., a mesh envelope[24] or spring clips **(SI: Additional Concepts: Spring-Based Jamming)**).

4. Conclusion

This paper demonstrates how the nonlinear structural phenomenon of laminar jamming can bridge the paradigms of soft robotics and traditional rigid robotics. We have derived an analytical model for two-layer jamming structures over all major phases of deformation, constructed highly accurate finite element models of many-layer laminar jamming structures, and extracted functional dependencies of major performance metrics on critical design inputs. We have demonstrated two novel functions, shape-locking and variable kinematics, that illustrate how laminar jamming can reversibly endow soft machines with behavior typical of traditional rigid robots. We also built a simple grasper capable of both pinch grasps and wrap grasps, demonstrating how laminar jamming can enhance the performance of real-world soft robotic systems. Collectively, our work elucidates the mechanics of laminar jamming, accelerates the design process of jamming structures, and provides a foundation for creating mechanically versatile machines and structures that cannot simply be categorized as “soft” or “rigid.”

5. Experimental Section

The following is an abridged description of the methods used in this study. For complete detail, see Supporting Information.

Analytical Modeling: The axial strain fields in each layer of the jamming structure were approximated as a superposition of a field that varied linearly with the vertical coordinate and a field that was constant with the vertical coordinate. An interfacial displacement variable was defined. Moment-stress relations and static equilibrium were used to derive governing equations for sections of the structure with cohesive interfaces and sections with slipped interfaces. Boundary conditions were formulated for clamped and free boundaries, and continuity conditions were defined to couple cohesive and slipped interfaces. The boundary-value problem was then explicitly solved to determine the elastica of a cantilevered jamming structure with a uniform distributed load in the pre-slip regime, transition regime, and full-slip regime. During the transition regime, the location of the transition between cohesive and slipped interfaces was also determined. The results were then used to derive stiffness, energy dissipation, and damping in each regime, as well as critical loads between the regimes. Dimensionless parameters were defined to nondimensionalize all results.

Finite Element Modeling: All finite element models were constructed using finite element simulation software (ABAQUS 6.14r2, Dassault Systèmes, Villacoublay, France). In the finite element models of the two-layer and many-layer jamming structures, each layer was approximated as a 2D plane-strain structure. Pressure equal to vacuum pressure was applied to all outer surfaces, and loads were subsequently applied. Large-deformation analysis was enabled, and the interfaces between the layers were defined as contact surfaces with a penalty friction formulation. A uniform mesh was used consisting of square four-node bilinear plane-strain quadrilateral elements with reduced integration. Each layer was meshed with two elements across its thickness.

In the finite element models of the variable kinematics structures, the rubber substrate and each of the jamming structures was modeled as a *homogeneous* 2D plane-strain structure. To simulate the vacuum-on condition, the elastic modulus of the jamming structure was

assigned to that of paper, and to simulate the vacuum-off condition, the modulus was reduced by a factor of $\boldsymbol{n^2}$, with $\boldsymbol{n = 20}$ to match experimental conditions. Cable actuation was approximated as a pure moment load. Large-deformation analysis was enabled. A uniform mesh was used consisting of square four-node bilinear plane-strain quadrilateral hybrid elements with reduced integration. The structure was meshed with four elements across its thickness.

Fabrication of Jamming Structures: The jamming structures were fabricated in five distinct steps. 1) Sheets of copy paper (HP Ultra White Multipurpose Copy Paper) were cut into strips on a laser cutter (VLS4.60, Universal Laser Systems, Inc., Scottsdale, AZ). 2) An acrylic frame enclosing the strips was cut on the laser cutter. The height of the acrylic frame was selected to be greater than the total thickness of the strips. The frame was used only for fabrication and did not comprise part of the jamming structure. 3) A sheet of thermoplastic polyurethane (TPU) (American Polyfilm, Inc., Branford, CT) was formed to the acrylic frame on a vacuum former (Formech 300XQ, Formech International Limited, Hertfordshire, UK). 4) The strips of paper and TPU tubing (Eldon James Corp., Denver, CO) were placed into the frame. The TPU sheet was folded over its contents, and the assembly was pressed in a heat press (Powerpress, Fancierstudio, Hayward, CA) at $\boldsymbol{100\ °C}$. Since the height of the acrylic frame was greater than the total thickness of the strips, the force of the heat press was concentrated on the frame; thus, only the region of the TPU sheet above the frame was sealed. The frame was then removed from the assembly. The remaining components comprised a jamming structure. 5) The end of the structure containing the TPU tubing was sandwiched between two conforming aluminum blocks. The blocks were heated to $\boldsymbol{171\ °C}$ on the heat press, creating a circumferential seal around the tubing. The blocks were then removed from the assembly.

Experimental Characterization: Jamming structures were tested on a three-point bending fixture in a universal materials testing device (Instron 5566, Illinois Tool Works, Norwood, MA). The structures were placed on the fixture and connected to a manual vacuum regulator (EW-07061-30, Cole-Parmer, Vernon Hills, IL) set to the desired pressure. The loading anvil of the testing device was lowered at a rate of $\mathbf{25}\ \boldsymbol{mm\ min^{-1}}$ until reaching the desired maximum displacement. Force and displacement measurements were simultaneously recorded.

Functions and Applications: All molds were designed using CAD software (Solidworks 2015, Dassault Systèmes, Villacoublay, France) and 3D printed using a stereolithography-based printer (Objet30 Scholar, Stratasys, Ltd., Eden Prairie, MN). For the actuator used in shape-locking demonstrations, a two-part mold was designed, and the actuator was cast from shore 10A platinum-cure silicone rubber (Dragon Skin 10 Medium, Smooth-On, Inc., Macungie, PA). The actuator and jamming structure were bonded using silicone building sealant (Dow Corning 795, Dow Corning, Midland, MI).

For the substrate used in the variable kinematics demonstrations, a one-part mold was designed with an inserted rod to create a channel for an actuation cable. The substrate was cast from high-stiffness PDMS rubber (Sylgard 184, Dow Corning, Midland, MI). The substrate and three-part jamming structure were again bonded using silicone building sealant. The cable consisted of braided polyethylene (Hollow Spectra, BHP Tackle, Harrington Park, NJ) and was tensioned using a turnbuckle mechanism.

For the fingertips of the fingers in the two-fingered grasper, a two-part mold was designed, and the fingertip was cast from shore 00-10A silicone rubber (Ecoflex 00-10, Smooth-On, Inc., Macungie, PA). Multi-axis stiffness tests and perturbation tests were

performed using a digital force gauge (Chatillon DFI10, AMETEK Sensors, Test & Calibration, Berwyn, PA) and custom-built fixtures.

Supporting Information
Supporting Information is available from the Wiley Online Library or from the author.

Acknowledgements
We would like to thank the members of the Harvard Biorobotics Laboratory; the Vlassak Group; the Harvard Biodesign Laboratory; the Bertoldi Group; and James Weaver, Ph.D., for their technical advice and assistance. Funding was provided by the National Science Foundation Graduate Research Fellowship Award 1122374 and the National Science Foundation National Robotics Initiative Grant CMMI-1637838.

Received: ((will be filled in by the editorial staff))
Revised: ((will be filled in by the editorial staff))
Published online: ((will be filled in by the editorial staff))

References

[1] K. Suzumori, S. Iikura, H. Tanaka, *IEEE Control Syst.* **1993**, *12*, 21.

[2] F. Iliesvki, A. D. Mazzeo, R. F.Shepherd, X. Chen, G. M. Whitesides, *Angew. Chem.* **2011**, *50*, 1890.

[3] O. A. Araromi, I. Gavrilovich, J. Shintake, S. Rosset, M. Richard, V. Gass, H. R. Shea, *IEEE/ASME Trans. Mechatronics* **2014**, *20*, 438.

[4] S. Shian, K. Bertoldi, D. Clarke, *Adv. Mater*. **2015**, *27*, 6814.

[5] R. V. Martinez, J. L. Branch, C. R. Fish, L. Jin, R. F. Shepherd, R.M.D. Nunes, Z. Suo, G. M. Whitesides, *Adv. Mater.* **2013**, *25*, 205.

[6] R. Deimel, O. Brock, *Int. J. Rob. Research* **2016**, *35*, 161.

[7] M. T. Tolley, R. F. Shepherd, B. Mosadegh, K. C. Galloway, M. Wehner, M. Karpelson, R. J. Wood, G. M. Whitesides, *Soft Rob.* **2014**, *1*, 213.

[8] P. Polygerinos, Z. Wang, K. C. Galloway, R. J. Wood, C. J. Walsh, *Rob. Auton. Syst.* **2015**, *73*, 135.

[9] M. Cianchetti, T. Ranzani, G. Gerboni, T. Nanayakkara, K. Althoefer, P. Dasgupta, A. Menciassi, *Soft Rob.* **2014**, *1*, 122.

[10] N. Cheng, G. Ishigami, S. Hawthorne, H. Chen, M. Hansen, M. Telleria, R. Playter, K. Iagnemma, in *Proc. IEEE Int. Conf. Rob. Autom. (ICRA)* **2010**, 5207.

[11] N. G. Cheng, A. Gopinath, L. Wang, K. Iagnemma, A. E. Hosoi, *Macromol. Mater. Eng.* **2014**, *299*, 1279.

[12] C. Laschi, M. Cianchetti, B. Mazzolai, L. Margheri, M. Follador, P. Dario, *Adv. Rob.* **2012**, *26*, 709.

[13] S. Seok, C. D. Onal, K.-J. Cho, R. J. Wood, D. Rus, S. Kim, *IEEE/ASME Trans. Mechatronics* **2013**, *18*, 1485.

[14] C. Majidi, R. J. Wood, *Appl. Phys. Lett.* **2010**, *97*, 164104.

[15] E. Brown, N. Rodenberg, J. Amend, A. Mozeika, E. Steltz, M. R. Zakin, H. Lipson, H. M. Jaeger, *Proc. Natl. Acad. Sci. U. S. A.* **2010**, *107*, 18809.

[16] M. Manti, V. Cacucciolo, M. Cianchetti, *IEEE Rob. Autom. Mag.* **2016**, *23*, 93.

[17] Y. Yang, Y. Chen, Y. Li, M. Z. Q. Chen, Y. Wei, *Soft Rob.* **2017**, *4*, 147.

[18] S. Kawamura, T. Yamamoto, D. Ishida, T. Ogata, Y. Nakayama, O. Tobata, S. Sugiyama, in *Proc. IEEE Int. Conf. Rob. Autom. (ICRA)* **2002**, 248**.**

[19] S. Kawamura, K. Kanaoka, Y. Nakayama, J. Jeon, D. Fujimoto, in *Proc. IEEE Int. Conf. Rob. Autom. (ICRA)* **2003**, 816.

[20] J. Ou, L. Yao, D. Tauber, J. Steimle, R. Niiyama, H. Ishii, in *Proc. 8th Int. Conf. Tangible Embedded Embodied Interact. (TEI)* **2014**, 65.

[21] M. Bureau, T. Keller, R. Velik, J. Perry, J. Veneman, in *Proc. IEEE Int. Conf. on Rehabil. Rob. (ICORR)* **2011**, 1.

[22] Y. J. Kim, S. Cheng, S. Kim, K. Iagnemma, *IEEE Trans. Rob.* **2013**, *29*, 1031.

[23] V. Wall, R. Deimel, O. Brock, in *Proc. IEEE Int. Conf. Rob. Autom. (ICRA)* **2015**, 252.

[24] J. L. C. Santiago, I. S. Godage, P. Gonthina, I. D. Walker, *Soft Rob.* **2016**, *3*, 54.

[25] Soft Robotics, http:/www.softroboticsinc.com/, accessed: January, 2018.

[26] L. U. Odhner, L. P. Jentoft, M. R. Claffee, N. Corson, Y. Tenzer, R. R. Ma, M. Buehler, R. Kohout, R. D. Howe, A. M. Dollar, *Int. J. Rob. Res.* **2014**, *33*, 736.

[27] Barrett Technology, LLC – Products – BarrettHand, http://www.barrett.com/products-hand.htm, accessed: January, 2018.

[28] M. Henke, G. Gerlach, *Microsyst. Technol.* **2014**, *20*, 599.

[29] T. P. Chenal, J. C. Case, J. Paik, R. K. Kramer, in *Proc. IEEE Int. Conf. Intell. Rob. Sys. (IROS)* **2014**, 2827.

[30] A. Tonazzini, S. Mintchev, B. Schubert, B. Mazzolai, J. Shintake, D. Floreano, *Adv. Mat.* **2016**, *28*, 10142.

[31] S. Rich, S.-H. Jang, Y.-L. Park, C. Majidi, *Adv. Mat. Technol.* **2017**, 1700179.

[32] C. Duriez, in *Proc. IEEE Int. Conf. Rob. Autom. (ICRA)* **2013**, 3982.

[33] G. Sumbre, G. Fiorito, T. Flash, B. Hochner, *Curr. Biol.* **2006**, *16*, 767.

[34] J. C. Case, E. L. White, R. K. Kramer, *Soft Rob.* **2015**, *2*, 80.

[35] Tensile properties of paper and paperboard (using constant rate of elongation apparatus), TAPPI T494, 2006.

[36] Coefficients of static and kinetic friction of uncoated writing and printing paper by use of the horizontal plane method, TAPPI T549, 2013.

[37] T. Yokoyama, K. Nakai, in *Conf. Expo. Exp. Appl. Mech.* **2007**.

[38] Paper Characteristics: Fuijtsu Quality Laboratory Limited, http://www.fujitsu.com/jp/group/fql/en/services/product-quality/analysis/method/paper/, accessed: January, 2018.

[39] A. D. Marchese, R. K. Katzschmann, D. Rus, *Soft Rob.* **2015**, *2*, 7.

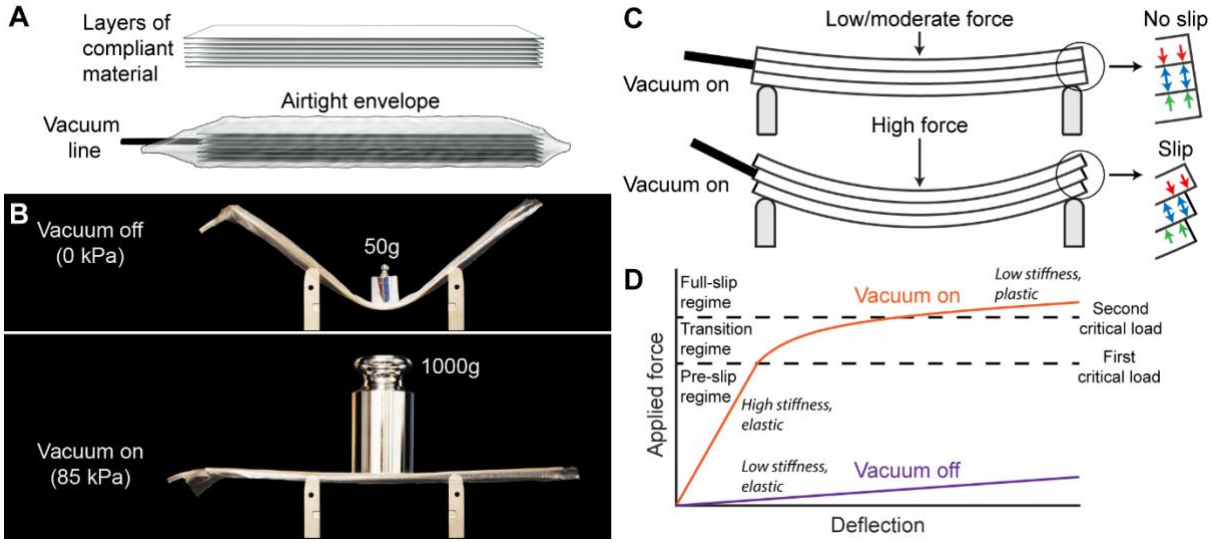

Figure 1. Fundamental behavior of laminar jamming structures. A) Schematic of a jamming structure. B) When vacuum is off, the layers bend independently, and the structure has low bending stiffness. When vacuum is on, the layers bend as a cohesive unit, and the structure has high bending stiffness. C) However, when vacuum is on, the layers are cohesive only until a critical force. For higher forces, longitudinal shear stress is large enough to cause the layers to slip at certain points along their interfaces. D) Summary of mechanical behavior. When vacuum is off, the structure has low bending stiffness, which is proportional to the slope of the curves. When vacuum is on, the structure has three deformation regimes. In *pre-slip*, the bending stiffness is maximal and constant. After the first critical load, the structure enters the *transition regime*, in which the layers begin to slip. The bending stiffness decreases. After the second critical load, the structure enters *full-slip*, in which the layers have slipped at all possible points along their interfaces. The bending stiffness is minimal and constant. When slip occurs, energy is dissipated to friction between the layers, and the structure behaves plastically.

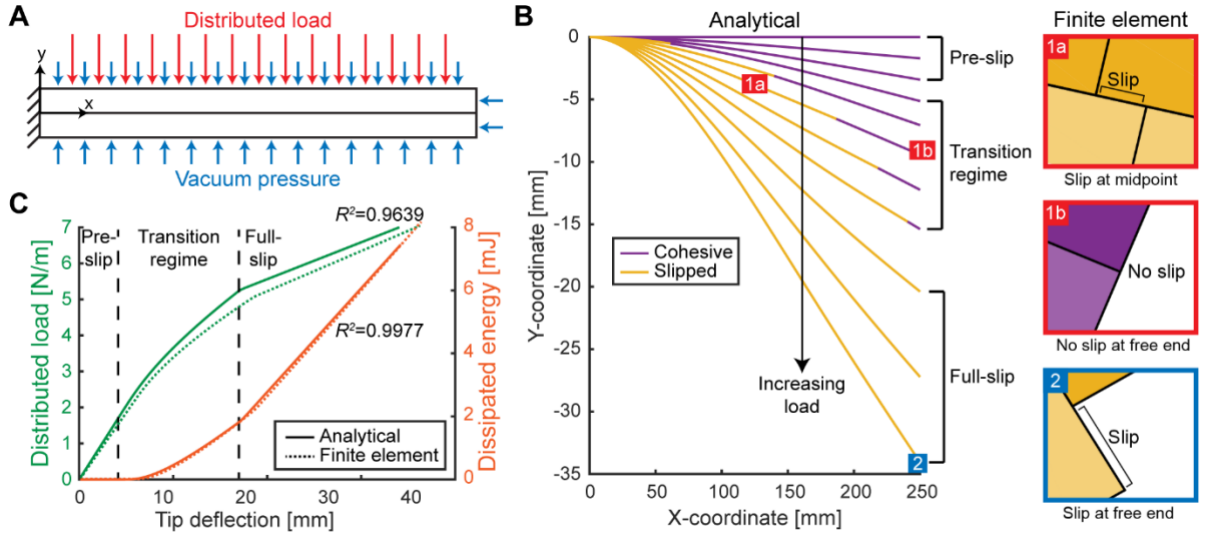

Figure 2. Analytical model of two-layer jamming structures. A) Schematic of example jamming structure. B) Elastica of jamming structure for increasing loads. The slipped region is highlighted at each load; because shear stress decreases along the x-direction, the slipped region initiates at the clamped end and grows toward the free end. Two-layer finite element models corroborated that slip occurred in analytically-predicted regions. C) Bending stiffness

is proportional to the slope of the load-versus-deflection curve; as expected, the stiffness transitions from a minimal to a maximal value. Damping is proportional to the slope of the dissipated-energy-versus-deflection curve; damping transitions from zero to a maximal value. Finite element models closely corroborated analytically-predicted stiffness and damping values. **(SI: Analytical Modeling: Case Study)**

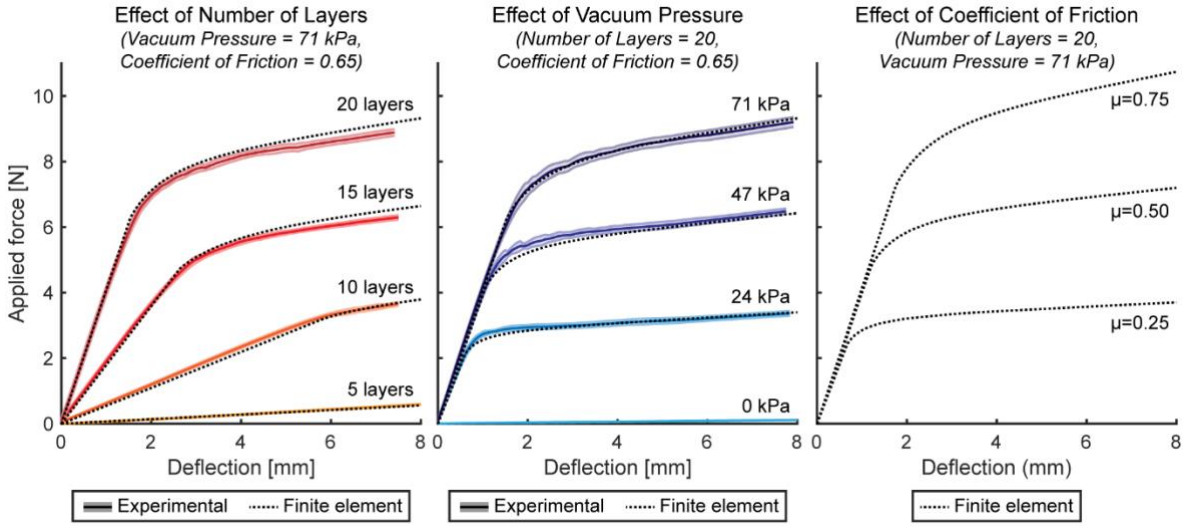

Figure 3. Finite element predictions and experimental validation for many-layer jamming structures. Jamming structures were loaded in three-point bending. Each experimental curve in fact consists of a mean curve and shaded error bar that spans ± 1 standard deviation; the maximum deviation on any curve is $0.24\ N$, indicating high repeatability. The minimum coefficient of determination (R^2) between finite element and experimental data is 0.9879, demonstrating exceptional predictive accuracy. (No experimental data is shown for coefficient of friction, as friction could not be precisely adjusted.) Hysteresis and damping predictions were experimentally evaluated as well **(Figure S6)**.

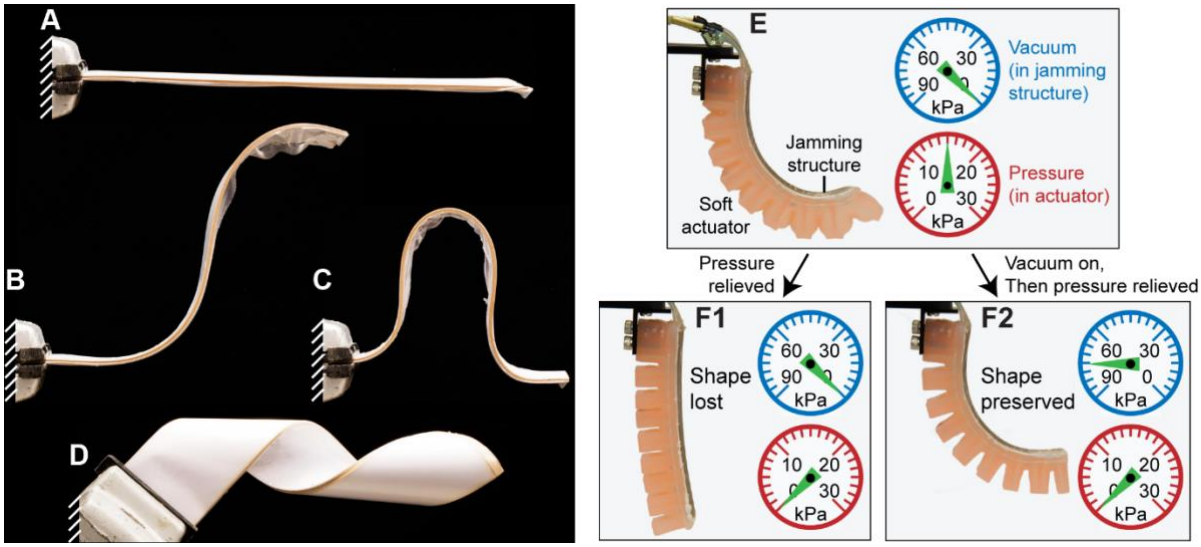

Figure 4. Demonstration of shape-locking function. A-D) A jamming structure consisting of twenty layers of copy paper was deformed into various shapes; vacuum was then applied, and the shape was preserved in all cases. E) A twenty-layer jamming structure was then adhered to a pneumatic soft actuator. The actuator was initially pressurized to $16\ kPa$ to achieve a desired bending angle. F1) In a first test, no vacuum was applied to the jamming structure,

and the actuator was depressurized. The composite structure immediately returned to its undeformed state. F2) In a second test, a vacuum pressure of 85 kPa was first applied to the jamming structure, and the actuator was then depressurized. Quantity R^2 between the arc of the ventral surface in E and the same arc in F2 was 0.9835. Thus, the system preserved its shape with high fidelity.

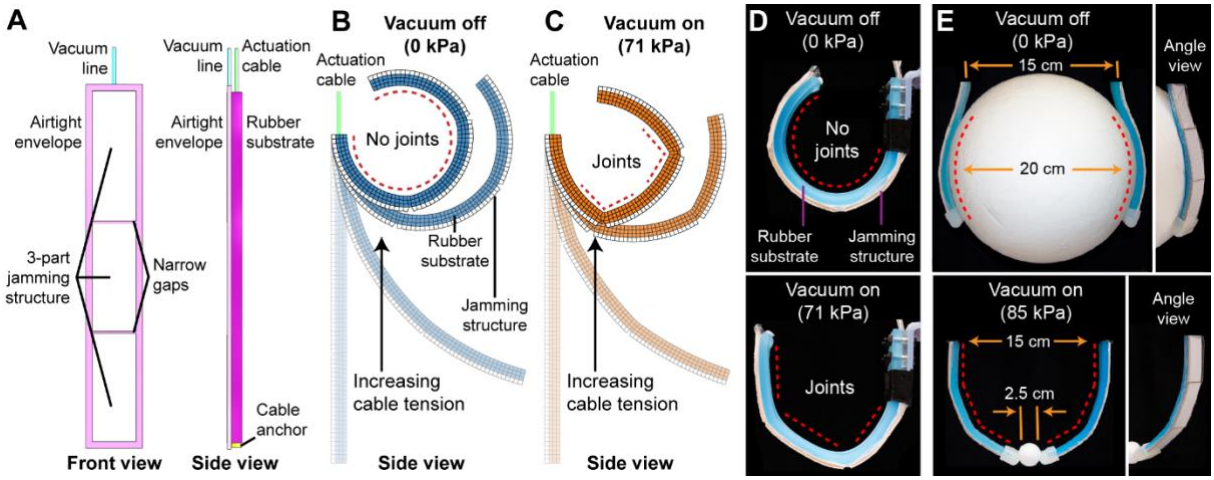

Figure 5. Finite element modeling and experimental demonstration of variable kinematics function. A) Schematic of variable kinematics system. B-C) Finite element simulations of variable kinematics behavior at increasing cable loads. At the highest load, the ratio of maximum to mean curvature increased by a factor of 6.65 with vacuum on, quantitatively verifying the creation of joints. D) Experimental validation of variable kinematics system. E) A two-fingered grasper was constructed in which each finger consisted of a variable kinematics system with a rounded fingertip. When no vacuum was applied to the fingers, the grasper could conform to a large ball, hold it aloft, and resist perturbation, thus performing a stable wrap grasp. When vacuum was applied, the grasper could perform a stable pinch grasp on a ball of one-eighth the diameter.

The laminar jamming phenomenon is used to bridge the paradigms of soft machines and traditional rigid robots. Analytical and finite element models of laminar jamming structures are developed and experimentally validated. Prototypes and simulations demonstrate that the structures can provide soft robotic systems with tunable stiffness, damping, and kinematics, including the ability to activate or deactivate joints on command.

Metamaterials

Y. S. Narang, J. J. Vlassak, R. D. Howe*

Mechanically Versatile Soft Machines Through Laminar Jamming

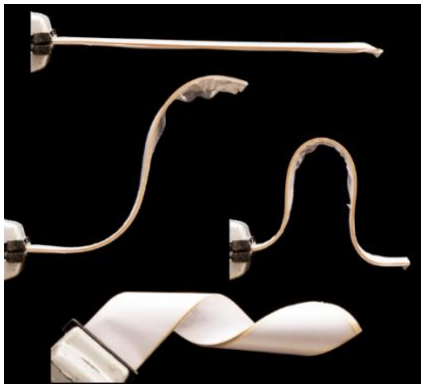

Supporting Information

Mechanically Versatile Soft Machines Through Laminar Jamming

*Yashraj S. Narang, Joost J. Vlassak, Robert D. Howe**

Analytical Modeling

Governing Equations

Consider a two-layer jamming structure. Let each layer be approximated as a thin beam with a width b, height h, length L, elastic modulus E, Poisson's ratio ν, and coefficient of friction μ.

Define a coordinate system with the origin located on the left edge of the structure at the interface between the layers (**Figure S1A**). Let the x-axis be horizontal (i.e., along the length of the undeformed structure), and let the y-axis be vertical (i.e., along the height of the undeformed structure).

Let the jamming structure be subject to a pressure gradient P. In this study, the jamming structure is actuated by enclosing the layers in an airtight envelope and applying a vacuum to the envelope. The pressure gradient P is equal to the vacuum pressure (i.e., the pressure in the envelope below ambient pressure). Thus, under standard atmospheric conditions, P has a maximum value of 1 atm.

Now let the jamming structure be loaded in the transverse direction. As the load increases, the longitudinal shear stress along the interface between the layers increases. At some regions of the interface, the longitudinal shear stress may be less than the maximum frictional stress (i.e., τ_f, which is equal to μP). These regions will remain cohesive (i.e., points that are initially coincident along the interface will remain coincident). On the other hand, at other regions of the interface, the longitudinal shear stress may equal the maximum frictional stress. These regions will slip (i.e., points that are initially coincident along the interface will move relative to each another), unless a boundary condition prevents slip from occurring.

We can write governing equations for cohesive sections of the jamming structure (i.e., sections of the jamming structure where the interface is cohesive) and slipped sections of the structure (i.e., sections of the jamming structure where the interface will slip, unless a boundary condition prevents slip from occurring).

Cohesive Sections

For cohesive sections of the jamming structure, we can write governing equations by directly using Euler-Bernoulli beam theory. The axial strain fields in the layers of the jamming structure are

$$\epsilon_1(x, y) = -\kappa(x)y$$

$$\epsilon_2(x,y) = -\kappa(x)y$$

where $\epsilon_1(x,y)$ and $\epsilon_2(x,y)$ are the axial strains in the bottom and top layers, respectively, and $\kappa(x)$ is the curvature along the interface.

Let us assume the layers are elastic and isotropic. The corresponding stress fields are

$$\sigma_1(x,y) = -E\kappa(x)y \quad (1)$$
$$\sigma_2(x,y) = -E\kappa(x)y \quad (2)$$

Note that when we later compare analytical results to finite element results, we substitute the plane-strain modulus $\bar{E} = \frac{E}{1-\nu^2}$ for the elastic modulus, as $b \gg h$ for the layers of the jamming structure that is investigated (**SI: Finite Element Model: Two-Layer Jamming Structure**).

We derive the first governing equation using the relationship between the resultant moment and the axial stress in the jamming structure (**Figure S1B**). The moment-stress relation for a single beam is given by $M(x) = \int_S -\sigma(x,y)y\, dS$, where $\sigma(x,y)$ is the axial stress and S is the cross-section of the beam. For a two-layer jamming structure,

$$M(x) = \int_{S_1} -\sigma_1(x,y)y\, dS_1 + \int_{S_2} -\sigma_2(x,y)y\, dS_2 \quad (3)$$

where S_1 and S_2 are the cross-sections of the bottom and top layers, respectively. Substituting equations (1) and (2),

$$M(x) = 2\kappa(x)EI \quad (4)$$

where I is the second moment of area of a cross-section of the top layer about the interface between the layers (i.e., $\frac{bh^3}{3}$). Equation (4) is the only governing equation for cohesive sections of the jamming structure.

Slipped Sections

In slipped sections of the jamming structure, each layer may have a distinct neutral axis, and the vertical location of each neutral axis may vary in the horizontal direction. Thus, we can describe the axial strain fields in the bottom and top layers as

$$\epsilon_1(x,y) = -\kappa(x)y + A_1(x) \quad (5)$$
$$\epsilon_2(x,y) = -\kappa(x)y + A_2(x) \quad (6)$$

where $A_1(x)$ and $A_2(x)$ are axial strain components that are introduced to allow the neutral axes of the layers to be distinct.

Again assuming the layers are elastic and isotropic, the corresponding stress fields are

$$\sigma_1(x,y) = -E\kappa(x)y + EA_1(x) \quad (7)$$
$$\sigma_2(x,y) = -E\kappa(x)y + EA_2(x) \quad (8)$$

Substituting into equation (3),

$$M(x) = 2\kappa(x)EI + \big(A_1(x) - A_2(x)\big)EJ \quad (9)$$

where J is the first moment of area of a cross-section of the top layer about the interface between the layers (i.e., $\frac{bh^2}{2}$).

We derive two more equations by performing static force equilibrium. From equilibrium of thin sections of the bottom layer (**Figure S1C**) and top layer (**Figure S1D**), respectively,

$$-\tau(x)bdx + \int_{S_1} \sigma_1(x+dx,y)\, dS_1 - \int_{S_1} \sigma_1(x,y)\, dS_1 = 0$$
$$\tau(x)bdx + \int_{S_2} \sigma_2(x+dx,y)\, dS_2 - \int_{S_2} \sigma_2(x,y)\, dS_2 = 0$$

where $\tau(x)$ is the shear stress exerted by the top surface of the bottom layer onto the bottom surface of the top layer. Substituting equations (7) and (8),

$$-\tau(x)b + EJ\frac{d\kappa}{dx} + ES_0\frac{dA_1}{dx} = 0$$
$$\tau(x)b - EJ\frac{d\kappa}{dx} + ES_0\frac{dA_2}{dx} = 0$$

where S_0 is the cross-sectional area of a single layer (i.e., bh).

In slipped sections of the jamming structure, $\tau(x) = \tau_f$. Substituting,

$$-\tau_f b + EJ\frac{d\kappa}{dx} + ES_0\frac{dA_1}{dx} = 0 \quad (10)$$
$$\tau_f b - EJ\frac{d\kappa}{dx} + ES_0\frac{dA_2}{dx} = 0 \quad (11)$$

Since the jamming structure is loaded in the transverse direction (and not in the axial direction), the integrals of axial stress over any cross-section should be zero. From equations (7) and (8), we find that $A_1(x) + A_2(x) = 0$. Thus, equations (9)-(11) can be simplified to

$$M(x) = 2\kappa(x)EI + 2A_1(x)EJ \quad (12)$$
$$-\tau_f b + EJ\frac{d\kappa}{dx} + ES_0\frac{dA_1}{dx} = 0 \quad (13)$$

Equations (12) and (13) are the two governing equations for slipped sections of the jamming structure.

Strain-Displacement Relations

Slipped Sections

For slipped sections of the jamming structure, it is useful to define variable $\delta_1(x)$ as the interfacial displacement for the bottom layer (i.e., the displacement of points along the top surface of the bottom layer) and variable $\delta_2(x)$ as the interfacial displacement for the top layer (i.e., the displacement of points along the bottom surface of the top layer).

From equations (5) and (6), the axial strain fields at the interface (i.e., at $y = 0$) simplify to $\epsilon_1(x) = A_1(x)$ and $\epsilon_2(x) = A_2(x)$. Thus, the interfacial displacements are related to $A_1(x)$ and $A_2(x)$ by the strain-displacement relations

$$\delta_1(x) = \int A_1(x)\, dx \tag{14}$$

$$\delta_2(x) = \int A_2(x)\, dx \tag{15}$$

Boundary Conditions

In practice, a jamming structure may be subject to one of several boundary conditions along its length (e.g., clamped, pinned, roller-supported, free). We provide clamped and free boundary conditions that will be relevant for our analysis of a cantilevered jamming structure. Additional boundary conditions can be readily derived for other physical scenarios.

Cohesive Sections

Clamped Conditions

Clamped boundary conditions at $x = a$ in cohesive sections of the jamming structure are

$$w(a) = 0 \tag{16}$$

$$\frac{dw}{dx}(a) = 0 \tag{17}$$

where $w(x)$ is the transverse deflection of the jamming structure at the interface (i.e., at $y = 0$).

Slipped Sections

Clamped Conditions

As in cohesive sections, clamped boundary conditions at $x = a$ in slipped sections of the jamming structure are

$$w(a) = 0 \tag{18}$$
$$\frac{dw}{dx}(a) = 0 \tag{19}$$

We can also formulate additional clamped boundary conditions for slipped sections that will be useful in our solution. At a clamped point, or at a boundary between slipped and cohesive sections, no interfacial displacements can occur. Thus,

$$\begin{aligned} \delta_1(a) &= 0 \\ \delta_2(a) &= 0 \end{aligned} \tag{20}$$

Free Conditions

For a free boundary at $x = b$, we know $\sigma_1(b, y) = \sigma_2(b, y) = 0$. Substituting into equations (7) and (8) and again noting that $A_1(x) + A_2(x) = 0$, we find the boundary condition

$$\kappa(b) = 0 \tag{21}$$

Continuity and Equilibrium

If a cohesive section and a slipped section of a jamming structure are adjacent, transverse deflections and slopes must be continuous. Symbolically, if the sections share a boundary at $x = c$,

$$w(c^-) = w(c^+) \tag{22}$$
$$\frac{dw}{dx}(c^-) = \frac{dw}{dx}(c^+) \tag{23}$$

In addition, axial stress is in equilibrium across the boundary (i.e., $\sigma_1(c^-, y) = \sigma_1(c^+, y)$ and $\sigma_2(c^-, y) = \sigma_2(c^+, y)$). Substituting equations (1), (2), (7), and (8) and evaluating at $y = 0$, we also find the conditions

$$\begin{aligned} A_1\left(c^{slip}\right) &= 0 \\ A_2\left(c^{slip}\right) &= 0 \end{aligned} \tag{24}$$

where c^{slip} denotes the slipped side of the boundary.

Explicit Solution

In general, for a vacuumed jamming structure subject to small loads, we expect that the longitudinal shear stress along all regions of the interface will be less than the maximum frictional stress. The jamming structure will remain entirely cohesive. We call this loading regime *pre-slip*.

As we progressively increase the load, we expect that the longitudinal shear stress along some regions of the interface will equal the maximum frictional stress. Along these regions, the layers will slip (except in areas where boundary conditions prevent slip from occurring), and along other regions, the layers will remain cohesive. We call this loading regime the *transition regime*.

Finally, past a certain load, we expect that the longitudinal shear stress along all regions of the interface will equal the maximum frictional stress. The jamming structure will be entirely slipped, except at regions of the interface where boundary conditions prevent slip from occurring. We call this loading regime *full-slip*.

We now solve the boundary problem for a typical jamming structure in each of these three loading regimes. We choose to analyze a cantilevered jamming structure clamped at $x = 0$ and subject to a uniform distributed load ω; such a case lucidly illustrates slip propagation (i.e., the gradual slip of adjacent layers along their interface), a mechanical phenomenon that jamming structures generally exhibit. (In contrast, a two-layer jamming structure in three-point bending would not exhibit slip propagation. Since longitudinal shear stress has a constant magnitude along the interface between the layers, the layers would slip along the full length of their interface at once.)

Specifically, we will provide explicit solutions for the deflection w, effective stiffness k, energy dissipated to friction E_{diss}, and effective damping d of the jamming structure. We define the effective stiffness as the incremental relationship between the distributed load and the deflection at the free end (i.e., $k = \frac{-\partial \omega}{\partial w(x=L)}$), and we define the effective damping as the incremental relationship between the dissipated energy and the deflection at the free end (i.e., $d = \frac{\partial E_{diss}}{\partial w(x=L)}$). (Note that ω is assumed to act in the negative y-direction; thus, positive ω results in negative w. The negative sign in k ensures that stiffness is positive as desired.)

Throughout the solution, we will use the small-deformation approximation $\kappa(x) \cong \frac{d^2w}{dx^2}$, where $\kappa(x)$ is the curvature of the jamming structure. This approximation allows the boundary-value problem to be explicitly solved, thus granting us deeper insight into the behavior of jamming structures. Note that when we later compare the results of the analytical model to the results of the finite element model (in which no small-deformation approximation is made), the analytical results still predict the finite element results with high accuracy (**SI: Finite Element Model: Two-Layer Jamming Structure**).

Resultant Shear and Moment

For a jamming structure clamped at $x = 0$ with a uniform distributed load ω, the resultant shear is

$$V(x) = \omega(L - x) \tag{25}$$

and the resultant moment is

$$M(x) = -\frac{\omega L^2}{2} + \omega\left(Lx - \frac{x^2}{2}\right) \tag{26}$$

Pre-slip Regime

Deflection

During pre-slip, the jamming structure is cohesive. Thus, we can start with governing equation (4). Substituting equation (26) into equation (4) and solving for $\frac{d^2w}{dx^2}$,

$$\frac{d^2w}{dx^2} = -\frac{\omega L^2}{4EI} + \frac{\omega L}{2EI}x - \frac{\omega}{4EI}x^2$$

Integrating twice,

$$w(x) = -\frac{\omega L^2}{8EI}x^2 + \frac{\omega L}{12EI}x^3 - \frac{\omega}{48EI}x^4 + C_1 x + C_2 \tag{27}$$

Applying clamped boundary conditions (18) and (19) at $x = 0$,

$$w(x) = -\frac{\omega L^2}{8EI}x^2 + \frac{\omega L}{12EI}x^3 - \frac{\omega}{48EI}x^4$$

which is a standard result from Euler-Bernoulli beam theory.

Substituting the explicit expression for I provided earlier (i.e., $I = \frac{bh^3}{3}$), we find the equivalent expression

$$w(x) = -\frac{3\omega L^2}{8Ebh^3}x^2 + \frac{\omega L}{4Ebh^3}x^3 - \frac{\omega}{16Ebh^3}x^4 \tag{28}$$

Stiffness, Dissipated Energy, and Damping

Substituting equation (28) into the definition of the effective stiffness of the jamming structure,

$$k = \frac{16Ebh^3}{3L^4} \tag{29}$$

Note that the effective stiffness is constant. Thus, the coefficient of friction and the vacuum pressure have no effect on the stiffness in the pre-slip regime.

Since there is no slip in the pre-slip regime, no energy is dissipated to friction. Thus, the dissipated energy and effective damping are

$$E_{diss} = 0 \tag{30}$$

$$d = 0 \tag{31}$$

Transition Regime

From equation (25), the resultant shear is maximum at the clamped end of the jamming structure and zero at the free end; thus, longitudinal shear stress is also maximum at the clamped end and zero at the free end. Therefore, we expect that the layers would begin slipping along their interface near the clamped end, and that the slipped region would grow until reaching the free end.

Thus, in the transition regime, we can divide the jamming structure into a slipped section and a cohesive section. Let χ be the value of x where the interface transitions from slipped to cohesive. We do not know χ a priori and will solve for its value.

Slipped Section ($0 \leq x \leq \chi$)

Deflection

To calculate $w(x)$ in the slipped section of the jamming structure in the transition regime, we first find general expressions for $A_1(x)$, $\delta_1(x)$, and $w(x)$.

We begin with $A_1(x)$. Solving for $\frac{dA_1}{dx}$ in governing equation (13) and integrating,

$$A_1(x) = \frac{\tau_f b}{ES_0}x - \frac{J}{S_0}\frac{d^2w}{dx^2} + C_2 \tag{32}$$

We proceed to $\delta_1(x)$. Substituting equation (32) into strain-displacement relation (14),

$$\delta_1(x) = \frac{\tau_f b}{ES_0}\frac{x^2}{2} - \frac{J}{S_0}\frac{dw}{dx} + C_2 x + C_1 \tag{33}$$

Finally, we proceed to $w(x)$. Substituting equation (26) into governing equation (12) and solving for $\frac{d^2w}{dx^2}$,

$$\frac{d^2w}{dx^2} = -\frac{\omega L^2}{4EI} + \frac{\omega}{2EI}\left(Lx - \frac{x^2}{2}\right) - \frac{J}{I}A_1(x)$$

Substituting equation (32),

$$\frac{d^2w}{dx^2}\left(1 - \frac{J^2}{S_0 I}\right) = -\frac{\omega L^2}{4EI} + \frac{\omega}{2EI}\left(Lx - \frac{x^2}{2}\right) - \frac{J}{I}\left(\frac{\tau_f b}{ES_0}x + C_2\right)$$

Integrating twice,

$$w(x)\left(1-\frac{J^2}{S_0 I}\right)=-\frac{\omega L^2}{4EI}\frac{x^2}{2}+\frac{\omega}{2EI}\left(L\frac{x^3}{6}-\frac{x^4}{24}\right)-\frac{J}{I}\left(\frac{\tau_f b}{ES_0}\frac{x^3}{6}+C_2\frac{x^2}{2}\right)+C_3x+C_4 \quad (34)$$

We can now apply clamped boundary conditions to equations (32)-(34) to explicitly solve for $w(x)$. Applying conditions (19) and (20) to equation (33) at $x=0$, we find $C_1=0$. Next, applying conditions (18) and (19) to equation (34) at $x=0$, we find $C_3=C_4=0$. Finally, applying conditions (24) and (20) to equations (32) and (33), respectively, at $x=\chi$,

$$0=\frac{\tau_f b}{ES_0}\chi-\frac{J}{S_0}\left.\frac{d^2w}{dx^2}\right|_{x=\chi}+C_2 \quad (35)$$

$$0=\frac{\tau_f b}{ES_0}\frac{\chi^2}{2}-\frac{J}{S_0}\left.\frac{dw}{dx}\right|_{x=\chi}+C_2\chi \quad (36)$$

These equations must be consistent with the expressions for $\left.\frac{dw}{dx}\right|_{x=\chi}$ and $\left.\frac{d^2w}{dx^2}\right|_{x=\chi}$ that can be derived from equation (34). Enforcing consistency and solving equations (35) and (36) for C_2 and χ, we find one trivial solution (where $\chi=0$) and one non-trivial solution. The non-trivial solution is

$$C_2=\frac{3\left(\tau_f b\right)^2 I}{4\omega ES_0 J}-\frac{\omega L^2 J}{16ES_0 I}-\frac{3\tau_f bL}{4ES_0} \quad (37)$$

$$\chi=\frac{3L}{2}-\frac{3\tau_f bI}{\omega J} \quad (38)$$

Substituting equation (37) into equation (34) and solving for $w(x)$, we find

$$w(x)=\frac{1}{1-\frac{J^2}{S_0 I}}\left(\left(\frac{\omega(LJ)^2}{32ES_0 I^2}+\frac{3\tau_f bLJ}{8ES_0 I}-\frac{3\left(\tau_f b\right)^2}{8\omega ES_0}-\frac{\omega L^2}{8EI}\right)x^2+\left(\frac{\omega L}{12EI}-\frac{\tau_f bJ}{6ES_0 I}\right)x^3-\frac{\omega}{48EI}x^4\right) \quad (39)$$

As desired, equation (39) is the deflection in the slipped section of the jamming structure in the transition regime. Equation (38) provides the length of the slipped section (i.e., the length of the slipped region along the interface between the layers) as a function of the distributed load and the maximum frictional stress.

If we substitute the explicit expressions for J, I, and τ_f provided earlier (i.e., $S_0=bh$, $J=\frac{bh^2}{2}$, $I=\frac{bh^3}{3}$, and $\tau_f=\mu P$) into equations (38) and (39) and simplify, we find the equivalent expressions

$$\chi=\frac{3L}{2}-\frac{2\mu Pbh}{\omega} \quad (40)$$

$$w(x) = \left(\frac{9\mu PL}{4Eh^2} - \frac{3(\mu P)^2 b}{2\omega Eh} - \frac{39\omega L^2}{32Ebh^3}\right)x^2 + \left(\frac{\omega L}{Ebh^3} - \frac{\mu P}{Eh^2}\right)x^3 - \frac{\omega}{4Ebh^3}x^4 \qquad (41)$$

This form of the expressions shows the exact functional dependence of the slipped length and the deflection on all critical design inputs (i.e., dimensions, material properties, the vacuum pressure, and the distributed load). Note that as the distributed load increases, the slipped length grows from a minimum value of zero to a maximum value of the length of the structure; the critical loads at which the slipped length begins and finishes growing are provided later in equations (56) and (57). In addition, the growth rate of the slipped length (i.e., $\frac{d\chi}{d\omega}$) scales with the vacuum pressure and the inverse square of the distributed load.

Stiffness, Dissipated Energy, and Damping

We previously defined the effective stiffness *k* of the jamming structure as the incremental relationship between the distributed load and the deflection at the tip. Since equation (41) is only valid for the slipped section of the jamming structure (i.e., for $0 \le x \le \chi$, where $\chi < L$), we do not yet know the deflection at the free end. Thus, we postpone the calculation of k to our subsequent investigation of the cohesive section.

Nevertheless, all the energy dissipated to friction in the transition regime arises in the slipped section, as no slip occurs in the cohesive section. Thus, we can calculate the dissipated energy E_{diss}.

We first compute $\delta_1(x)$ and $\delta_2(x)$. Substituting equation (37), equation (39), and the result $C_1 = 0$ all into equation (33),

$$\delta_1(x) = \frac{1}{\left(1 - \frac{J^2}{S_0 I}\right)} \frac{\left(36(\tau_f bI)^2 - 36\omega\tau_f bLJI + 9(\omega LJ)^2\right)x + \left(24\omega\tau_f bJI - 12(\omega J)^2 L\right)x^2 + 4(\omega J)^2 x^3}{48\omega E S_0 JI} \qquad (42)$$

From the earlier result $A_1(x) + A_2(x) = 0$ and the clamped boundary condition $\delta_2(0) = 0$, we find the intuitive result $\delta_2(x) = -\delta_1(x)$. We can define $\delta_r(x)$ as the relative displacement between points that were initially coincident on the interface (i.e., $\delta_1(x) - \delta_2(x)$). Thus, $\delta_r(x) = 2\delta_1(x)$.

The dissipated energy E_{diss} is the local frictional force per unit length at the interface, multiplied by the relative interfacial displacement, integrated over the length of the slipped section. Symbolically,

$$E_{diss} = \int_0^{\chi} \tau_f b \delta_r(x) dx \tag{43}$$

Substituting $\delta_r(x)$,

$$E_{diss} = \frac{1}{\left(1 - \frac{J^2}{S_0 I}\right)} \frac{36\left(\tau_f b\right)^3 (\chi I)^2 + 4\omega\left(\tau_f b \chi\right)^2 JI(4\chi - 9L) + \omega^2 \tau_f b (\chi J)^2 (9L^2 - 8L\chi + 2\chi^2)}{48\omega E S_0 JI}$$

Substituting the explicit expressions for I, J, τ_f, and χ, we find the equivalent expression

$$E_{diss} = \frac{256(\mu P)^5 (bh)^4 - 768\omega L(\mu P)^4 (bh)^3 + 864(\omega L bh)^2 (\mu P)^3 - 432(\omega L)^3 (\mu P)^2 bh + 81(\omega L)^4 \mu P}{192\omega^3 E h^2} \tag{44}$$

This form of the expression shows the exact functional dependence of the dissipated energy in the transition regime on all critical design inputs (i.e., dimensions, material properties, the vacuum pressure, and the distributed load).

Finally, as described earlier, we define the effective damping d as the incremental relationship between E_{diss} and the maximum deflection. From the chain rule, we know that $\frac{\partial E_{diss}}{\partial w(x=L)} = \frac{\partial E_{diss}}{\partial \omega} \frac{\partial \omega}{\partial w(x=L)}$. Simplifying, $d = -k \frac{\partial E_{diss}}{\partial \omega}$. Again, we cannot yet calculate d of the jamming structure in the transition regime, as we have had to postpone our calculation of k to the subsequent investigation of the cohesive section.

Cohesive Section ($\chi \leq x \leq L$):

Deflection

To solve for $w(x)$ in the cohesive section of the jamming structure in the transition regime, we may begin with equation (27). Repeating for clarity,

$$w(x) = -\frac{\omega L^2}{8EI} x^2 + \frac{\omega L}{12EI} x^3 - \frac{\omega}{48EI} x^4 + C_1 x + C_2 \tag{45}$$

Applying continuity boundary conditions (22) and (23) at $x = \chi$, we find $C_1 = 0$,

$$C_2 = \frac{1}{S_0 I - J^2} \left(\frac{-9\omega L^4 J^2}{256EI} + \frac{9\tau_f b L^3 J}{32E} - \frac{27\left(\tau_f b L\right)^2 I}{32\omega E} + \frac{9\left(\tau_f b\right)^3 L I^2}{8\omega^2 EJ} - \frac{9\left(\tau_f b\right)^4 I^3}{16\omega^3 EJ^2} \right)$$

and

$$w(x) = -\frac{\omega L^2}{8EI}x^2 + \frac{\omega L}{12EI}x^3 - \frac{\omega}{48EI}x^4 + \frac{1}{S_0 I - J^2}\left(\frac{-9\omega L^4 J^2}{256EI} + \frac{9\tau_f b L^3 J}{32E} - \frac{27\left(\tau_f b L\right)^2 I}{32\omega E} + \frac{9\left(\tau_f b\right)^3 L I^2}{8\omega^2 E J} - \frac{9\left(\tau_f b\right)^4 I^3}{16\omega^3 E J^2}\right)$$

Substituting the explicit expressions for I, J, and τ_f, we find

$$w(x) = -\frac{3\omega L^2}{8Ebh^3}x^2 + \frac{\omega L}{4Ebh^3}x^3 - \frac{\omega}{16Ebh^3}x^4 + \frac{27\mu P L^3}{16Eh^2} - \frac{(\mu P)^4 b^3 h}{\omega^3 E} + \frac{3(\mu P)^3 b^2 L}{\omega^2 E} - \frac{27(\mu P)^2 b L^2}{8\omega E h} - \frac{81\omega L^4}{256Ebh^3} \quad (46)$$

Stiffness, Dissipated Energy, and Damping

As equation (46) is valid for the cohesive section of the jamming structure (i.e., for $\chi \leq x \leq L$), we now know the deflection at the free end in the transition regime and can calculate the effective stiffness k. Substituting equation (46) into the definition of k,

$$k = \frac{-256\omega^4 Ebh^3}{768(\mu Pbh)^4 - 1536\omega L(\mu Pbh)^3 + 864(\omega L\mu Pbh)^2 - 129(\omega L)^4} \quad (47)$$

Note that the effective stiffness of the jamming structure in the transition regime is a function of both the distributed load and the vacuum pressure.

We can now solve for the effective damping d of the jamming structure in the transition regime as well. Substituting equations (47) and (44) into the earlier result $d = -k\frac{\partial E_{diss}}{\partial \omega}$,

$$d = \frac{1024(\mu Pbh)^5 - 2048\omega L(\mu Pbh)^4 + 1152(\omega L)^2(\mu Pbh)^3 - 108(\omega L)^4 \mu Pbh}{768(\mu Pbh)^4 - 1536\omega L(\mu Pbh)^3 + 864(\omega L\mu Pbh)^2 - 129(\omega L)^4} \quad (48)$$

Note that the effective damping of the jamming structure in the transition regime is a function of both the distributed load and the vacuum pressure as well.

Full-slip Regime

Deflection

To solve for $w(x)$ of the jamming structure in the full-slip regime, we may begin with equation (32), as well as equation (34) after applying clamped boundary conditions (18) and (19) at $x = 0$. Providing for clarity,

$$A_1(x) = \frac{\tau_f b}{ES_0}x - \frac{J}{S_0}\frac{d^2w}{dx^2} + C_2 \tag{49}$$

$$w(x)\left(1 - \frac{J^2}{S_0 I}\right) = -\frac{\omega L^2}{4EI}\frac{x^2}{2} + \frac{\omega}{2EI}\left(L\frac{x^3}{6} - \frac{x^4}{24}\right) - \frac{J}{I}\left(\frac{\tau_f b}{ES_0}\frac{x^3}{6} + C_2\frac{x^2}{2}\right) \tag{50}$$

We cannot apply continuity boundary conditions (22) and (23), as the entire interface has slipped and the value of χ has now exceeded the length of the structure. However, we may apply free boundary condition (21) at $x = L$. Evaluating, we find $C_2 = \frac{-\tau_f bL}{ES_0}$. Substituting into equation (50) and solving for $w(x)$,

$$w(x) = \frac{1}{1 - \frac{J^2}{S_0 I}}\left(\left(\frac{\tau_f bLJ}{2ES_0 I} - \frac{\omega L^2}{8EI}\right)x^2 + \left(\frac{\omega L}{12EI} - \frac{\tau_f bJ}{6ES_0 I}\right)x^3 - \frac{\omega}{48EI}x^4\right) \tag{51}$$

Substituting the explicit expressions for I, J, and τ_f, we find the equivalent expression

$$w(x) = \left(\frac{3\mu PL}{Eh^2} - \frac{3\omega L^2}{2Ebh^3}\right)x^2 + \left(\frac{\omega L}{Ebh^3} - \frac{\mu P}{Eh^2}\right)x^3 - \frac{\omega}{4Ebh^3}x^4 \tag{52}$$

Note that the deflection of the jamming structure in the full-slip regime is a function of the coefficient of friction and the vacuum pressure. In contrast, the deflection of a two-layer structure with a frictionless interface (or equivalently, the deflection of a two-layer structure when no vacuum is applied) is $w(x) = -\frac{3\omega L^2}{2Ebh^3}x^2 + \frac{\omega L}{Ebh^3}x^3 - \frac{\omega}{4Ebh^3}x^4$, which depends on neither the coefficient of friction nor the vacuum pressure.

Stiffness, Dissipated Energy, and Damping

Substituting equation (52) into the definition of the effective stiffness of the jamming structure,

$$k = \frac{4Ebh^3}{3L^4} \tag{53}$$

Note that the effective stiffness of the jamming structure in the full-slip regime is constant. In addition, this stiffness is equal to the effective stiffness of a two-layer structure with a frictionless interface (or equivalently, the stiffness of a two-layer structure when no vacuum is applied).

Analogous to the slipped section of the transition regime, to calculate E_{diss}, we first compute $\delta_r(x)$. We may begin with equation (33). Repeating for clarity,

$$\delta_1(x) = \frac{\tau_f b}{ES_0}\frac{x^2}{2} - \frac{J}{S_0}\frac{dw}{dx} + C_2 x + C_1$$

Applying clamped boundary conditions (19) and (21) at $x = 0$, we find $C_1 = 0$. Substituting equation (52) and the earlier result $C_2 = \frac{-\tau_f bL}{ES_0}$,

$$\delta_1(x) = \frac{1}{\left(1 - \frac{J^2}{S_0 I}\right)} \frac{\left(3\omega L^2 J - 12\tau_f bLI\right)x + \left(6\tau_f bI - 3\omega LJ\right)x^2 + \omega J x^3}{12ES_0 I}$$

As before, $\delta_r(x) = 2\delta_1(x)$. Substituting into equation (43) with $\chi = L$,

$$E_{diss} = \frac{1}{\left(1 - \frac{J^2}{S_0 I}\right)} \frac{3\omega\tau_f bL^4 J - 16\left(\tau_f b\right)^2 L^3 I}{24ES_0 I}$$

Substituting the explicit expressions for I, J, and τ_f, we find the equivalent expression

$$E_{diss} = \frac{9\omega\mu PL^4 - 32(\mu P)^2 bhL^3}{12Eh^2} \tag{54}$$

Note that the dissipated energy in the full-slip regime is a function of both the distributed load and the vacuum pressure.

Finally, substituting equations (53) and (54) into the simplified expression for the effective damping of the jamming structure (i.e., $d = -k\frac{\partial E_{diss}}{\partial \omega}$), we find

$$d = \mu P b h \tag{55}$$

Note that the effective damping of the jamming structure in the full-slip regime is independent of the distributed load, but scales with the vacuum pressure. This result suggests that damping may be controlled in a real-world jamming structure over a continuum of values by forcing the structure into the full-slip regime and varying vacuum pressure as desired. This concept is investigated later for many-layer jamming structures (**SI: Additional Concepts: Continuously-Variable Damping**).

Transition Loads Between Regimes

Let us define the *first transition load* ω_1 to be the load at which the jamming structure shifts from the pre-slip regime to the transition regime. The first transition load can be found by solving equation (40) for ω when $\chi = 0$. Explicitly,

$$\omega_1 = \frac{4\mu P b h}{3L} \tag{56}$$

Let us define the *second transition load* ω_2 to be the load at which the jamming structure shifts from the transition regime to the full-slip regime. The second transition load can be found by solving equation (40) for ω when $\chi = L$. Explicitly,

$$\omega_2 = \frac{4\mu P b h}{L} \tag{57}$$

Summary of Formulae

Equation (28) describes the deflection of the two-layer jamming structure during the pre-slip regime, and equation (29) describes the effective stiffness of the structure in this regime. Equations (30) and (31) describe the dissipated energy and the effective damping, which are zero.

Equations (40), (41), and (46) describe the deflection of the jamming structure during the transition regime (in both the slipped and cohesive sections of the structure), and equation (47) describes the effective stiffness of the structure in this regime. Equations (44) and (48) describe the dissipated energy and the effective damping, respectively.

Equation (52) describes the deflection of the structure during the full-slip regime, and equation (53) describes the effective stiffness of the two-layer structure during this regime. Equations (54) and (55) describe the dissipated energy and the effective damping, respectively.

Finally, equations (56) and (57) describe the loads at which the jamming structure shifts between consecutive regimes.

Thus, we have formulated a complete model for the kinematics, stiffness, dissipated energy, and damping of a two-layer jamming structure over all major phases of deformation.

Dimensionless Forms

Through nondimensionalization, all the preceding formulae can be dramatically simplified. We can define dimensionless variables $w^* = \frac{w}{L}$, $x^* = \frac{x}{L}$, $k^* = \frac{k}{E}$, $E^*_{diss} = \frac{E_{diss}}{EL^3}$, $d^* = \frac{d}{EL^2}$, $\omega^* = \frac{\omega}{EL}$, $\mu^* = \mu$, $P^* = \frac{P}{E}$, $b^* = \frac{b}{L}$, and $h^* = \frac{h}{L}$. We can also define the composite dimensionless variables $\alpha^* = b^* h^{*3}$ and $\beta^* = \mu^* P^* b^* h^*$. Substituting these variables into the formulae, we find the following dimensionless formulae:

Pre-slip Regime

$$w^* = \frac{-3\omega^*}{8\alpha^*} x^{*2} + \frac{\omega^*}{4\alpha^*} x^{*3} - \frac{\omega^*}{16\alpha^*} x^{*4}$$

$$k^* = \frac{16\alpha^*}{3}$$

$$E^*_{diss} = 0$$

$$d^* = 0$$

Transition Regime

$$k^* = \frac{-256\omega^{*4}\alpha^*}{768\beta^{*4} - 1536\omega^*\beta^{*3} + 864\omega^{*2}\beta^{*2} - 129\omega^{*4}}$$

$$E^*_{diss} = \frac{256\beta^{*5} - 768\omega^*\beta^{*4} + 864\omega^{*2}\beta^{*3} - 432\omega^{*3}\beta^{*2} + 81\omega^{*4}\beta^*}{192\omega^{*3}\alpha^*}$$

$$d^* = \frac{1024\beta^{*5} - 2048\omega^*\beta^{*4} + 1152\omega^{*2}\beta^{*3} - 108\omega^{*4}\beta^*}{768\beta^{*4} - 1536\omega^*\beta^{*3} + 864\omega^{*2}\beta^{*2} - 129\omega^{*4}}$$

Slipped Section

$$\chi^* = \frac{3}{2} - \frac{2\beta^*}{\omega^*}$$

$$w^* = \left(\frac{9\beta^*}{4\alpha^*} - \frac{3\beta^{*2}}{2\omega^*\alpha^*} - \frac{39\omega^*}{32\alpha^*}\right)x^{*2} + \left(\frac{\omega^*}{\alpha^*} - \frac{\beta^*}{\alpha^*}\right)x^{*3} - \frac{\omega^*}{4\alpha^*}x^{*4}$$

Cohesive Section

$$w^* = \frac{-3\omega^*}{8\alpha^*}x^{*2} + \frac{\omega^*}{4\alpha^*}x^{*3} - \frac{\omega^*}{16\alpha^*}x^{*4} + \frac{27\beta^*}{16\alpha^*} - \frac{\beta^{*4}}{\omega^3\alpha^*} + \frac{3\beta^{*3}}{\omega^{*2}\alpha^*} - \frac{27\beta^{*2}}{8\omega^*\alpha^*} - \frac{81\omega^*}{256\alpha^*}$$

Full-slip Regime

$$w^* = \left(\frac{3\beta^*}{\alpha^*} - \frac{3\omega^*}{2\alpha^*}\right)x^{*2} + \left(\frac{\omega^*}{\alpha^*} - \frac{\beta^*}{\alpha^*}\right)x^{*3} - \frac{\omega^*}{4\alpha^*}x^{*4}$$

$$k^* = \frac{4\alpha^*}{3}$$

$$E^*_{diss} = \frac{9\omega^*\beta^* - 32\beta^{*2}}{12\alpha^*}$$

$$d^* = \beta^*$$

Transition Loads

$$\omega_1^* = \frac{4\beta^*}{3}$$

$$\omega_2^* = 4\beta^*$$

Note that dimensionless deflections are found to depend on at most 4 dimensionless parameters (i.e., ω^*, x^*, α^*, and β^*); dimensionless stiffnesses and dissipated energies depend on at most 3 parameters (i.e., ω^*, α^*, and β^*); dimensionless damping values depend on at most 2 parameters (i.e., ω^* and β^*); and dimensionless transition loads depend on just 1 parameter (i.e., β^*).

Case Study

The analytical model was evaluated for an example two-layer jamming structure. Each layer had dimensions $b = 50\ mm$, $h = 0.1\ mm$, and $L = 250\ mm$, as well as a Poisson's ratio $v = 0.156$ and coefficient of friction $\mu = 0.65$. These dimensions and material properties coincided with those of the real-life jamming structures examined later during experimental characterization (**SI: Experimental Characterization: Characterization Process**).

If a two-layer jamming structure with the above properties consisted of compliant material, it would not slip until the structure exhibited exceptionally large deflections. Thus, the elastic modulus E was set to $6\ TPa$ in order to illustrate slip over a more reasonable range of deflection. In addition, as described earlier, the plane-strain modulus $\bar{E} = \frac{E}{1-v^2}$ was substituted for the elastic modulus in the analytical formulae, as $b \gg h$.

A vacuum pressure $P = 101\ kPa$ was imposed, and a uniform distributed load $\omega = 7\frac{N}{m}$ was applied over 100 equal increments. The elastica (i.e., shape), the deflection at the free end of the jamming structure, and the dissipated energy were computed for each load increment.

Curvature Reversal

For a typical cantilever beam under a uniform distributed load, the curvature of the beam maintains a consistent sign. However, for a two-layer jamming structure, the analytical model predicts that the curvature reverses (i.e., changes sign) along its length at moderate loads and higher. Curvature reversal can be seen on close inspection of the elastica in the case study (**Figure 2B**).

The analytical model in the transition regime may provide a first explanation of this counterintuitive phenomenon. Because the net force on any cross section is zero, $A_1(x) + A_2(x) = 0$ for all x. Furthermore, because the jamming structure is cohesive for $\chi \leq x < L$, interfacial displacements must be zero at $x = \chi$. Thus, positive values of $A_1(x)$ within the slipped section of the jamming structure (i.e., $0 \leq x \leq \chi$) must be balanced by negative values of $A_1(x)$ elsewhere in the slipped section; likewise, positive values of $A_2(x)$ must be balanced by negative values of $A_2(x)$. Equations (5) and (6) imply a similar (but not identical) relationship for $\kappa(x)$.

Curvature reversal was corroborated in detail by finite element models of two-layer jamming structures, as well as finite element models and experimental observations of many-layer jamming structures (**SI: Finite Element Modeling: Two-Layer Jamming Structures**).

Extending the Model

The analytical modeling procedure for two-layer jamming structures can be adapted to solve for the deflection of jamming structures with arbitrary numbers of layers and arbitrary boundary conditions.

Arbitrary Numbers of Layers

Three important results may be simply derived for many-layer jamming structures. First, the elastica of a vacuumed jamming structure during the pre-slip regime can be determined by approximating the structure as a cohesive thin beam and directly using Euler-Bernoulli beam theory to calculate deflection.

Second, as cited in the main text, the bending stiffness of a vacuumed many-layer jamming structure during the pre-slip regime is a factor of n^2 greater than the stiffness when no vacuum is applied, where n is the number of layers.[18] This result can be derived from second area moments of inertia. When a vacuumed jamming structure is in the pre-slip regime, the structure is cohesive, and the second area moment of inertia of the jamming structure is given by $I = \frac{b(nh)^3}{12} = n^3\frac{bh^3}{12}$. When no vacuum is applied to a jamming structure, the layers are decoupled, and $I = n\frac{bh^3}{12}$. Since bending stiffness is proportional to I, the stiffness in the former case is a factor of n^2 greater than that in the latter case.

Third, the first transition load (i.e., the load at which a jamming structure shifts from the pre-slip regime to the transition regime) for many layer-jamming structures is given by $V_{max} = \frac{2\mu PA}{3}$, where V_{max} is the maximum resultant shear at any cross-section of the beam, which is proportional to the applied load; and A is the total cross-sectional area (i.e., nbh).[28] This result can be derived from the definition of slip. Slip occurs when the maximum longitudinal shear stress at an interface equals the maximum possible shear stress. During the pre-slip regime, the maximum longitudinal shear stress occurs at the innermost interface and is given by the well-known formula $\tau_{max} = \frac{3V_{max}}{2A}$. Furthermore, the maximum possible shear stress is μP. Equating the two expressions and solving for V_{max}, we see $V_{max} = \frac{2\mu PA}{3}$.

Despite the simplicity of deriving the previous three results, solving for the deformation of a many-layer jamming structure during the transition regime and full-slip regime is a far greater challenge. This paper has provided detailed methods for solving for the deformation of a two-layer jamming structure during these regimes; these methods may be extended to solve the many-layer problem as well.

For a many-layer jamming structure, strain distributions can again be defined for each layer as the superposition of a linear strain term and a unique axial strain term. The moment-stress relation can be used to derive a first governing equation. Static force equilibrium can then be performed on thin sections of each layer to derive subsequent governing equations. For the outermost layers, these equations would be similar to equations (10) and (11) for the two-layer jamming structure; for inner layers, shear stress would act on both the top and bottom surfaces of the thin section, producing a second shear stress term.

Whereas slip propagates along one dimension (i.e., along the x-axis, as defined in **Figure S1A**) for a two-layer jamming structure, slip would propagate along two dimensions (i.e., along the x- and y-axes) for a many-layer jamming structure. Shear stress varies through the thickness of the structure, and slip would occur along distinct interfaces at disparate loads. Thus, a unique χ variable would be required for each interface. Moreover, boundary conditions (24) and (20) would only be valid at $x = \chi$ if χ corresponded to an interface located along the x-axis; for other interfaces, alternative boundary conditions would need to be formulated. For example, continuity of incremental interfacial displacements and axial strains may be enforced.

Although the process of solving for the deflection of a many-layer jamming structure is straightforward, the solution itself may be algebraically taxing. Furthermore, the analytical solution would only be valid for small deflections. Thus, numerical solutions (e.g., finite element analysis) may be far more convenient.

Arbitrary Boundary Conditions

For arbitrary boundary conditions, the direction of shear stress and frictional stress may change along the length of an interface. Thus, the signs in the governing equations based on static force equilibrium may vary throughout the jamming structure. Furthermore, each interface may consist of multiple slipped and cohesive regions. More than one χ variable would be necessary for each interface, along with continuity boundary conditions between adjacent slipped and cohesive sections of the structure.

Finite Element Modeling

All finite element models were constructed using finite element simulation software (ABAQUS 6.14r2, Dassault Systèmes, Villacoublay, France). Analysis of simulation results was performed using numerical computing software (MATLAB 2017a, MathWorks, Natick, MA).

Two-Layer Jamming Structures

A finite element model was constructed for a two-layer jamming structure. Each layer was approximated as a 2D plane-strain structure, and the jamming structure had dimensions, material properties, vacuum pressure, and distributed load equal to those specified in the case study for the analytical model of a two-layer jamming structure (**SI: Analytical Modeling: Case Study**).

Boundary conditions and loads were also identical to those used in the case study. First, pressure (equal to the vacuum pressure) was applied to all outer surfaces of the jamming structure; then, the uniform distributed load was applied as a ramp over 100 equal increments. Large-deformation analysis was enabled. The interface between the two layers was chosen to be a contact surface with a penalty friction formulation. To mitigate undesired simulation of elastic slip, the slip tolerance was set to $5 * 10^{-5}$. A uniform mesh was used that consisted of square four-node bilinear plane-strain quadrilateral elements with reduced integration (CPE4R). Each layer had two elements across its thickness. A mesh refinement study was conducted later for many-layer jamming structures to ensure that a finer mesh was not required (**SI: Finite Element Modeling: Stiffness of Many-Layer Jamming Structures**). The elastica, deflection at the free end, and dissipated energy were extracted at each load increment.

The analytical model predicted finite element results for a two-layer jamming structure with high accuracy (**Figure S2A-C**). Elastica were predicted with coefficients of determination (R^2) between 0.9207 and 0.9759. Furthermore, the load-versus-deflection curve of the structure was predicted with $R^2 = 0.9639$, and the dissipated-energy-versus-deflection curve was predicted with $R^2 = 0.9977$. Note that finite element models of many-layer jamming structures were later found to predict experimental results with exceptional accuracy; thus, the analytical model was deemed predictive of real-world jamming structures as well.

The curvature reversal phenomenon predicted by the analytical model (**SI: Analytical Modeling: Curvature Reversal**) was also corroborated by the finite element results (**Figure S2D-E**). For the analytical model, curvatures were computed for each of the analytical elastica in **Figure S2A** using appropriate first and second derivatives of the formulae for deflection (**SI: Analytical Modeling: Summary of Formulae**). For the finite element model, fourth-order best-fit polynomials were first determined for each of the finite element elastica in **Figure S2A**. Curvatures were then computed using appropriate first and second derivatives of the best-fit polynomials. The analytical curvature profiles (**Figure S2D**) were visually predictive of the finite element curvature profiles (**Figure S2E**), including the x-coordinates at which curvature reversal occurred.

Curvature reversal was also observed later for both finite element models and experimental samples of many-layer jamming structures in three-point bending (**Figure S2F**).

Stiffness of Many-Layer Jamming Structures

Finite element models of many-layer jamming structures were constructed according to the same process used for two-layer jamming structures; however, the structures were loaded in three-point bending. Rollers (i.e., zero-vertical-displacement boundary conditions) were applied to two points on the bottom surface, $60\ mm$ from either side; the location of these virtual rollers coincided with the location of the rollers used later during experimental characterization. In addition, to stabilize the finite element model, a zero-horizontal-displacement boundary condition was applied at the center of the top surface of the structure.

After applying pressure to all outer surfaces of the jamming structure, a concentrated transverse displacement was applied to the midpoint of the top surface. The displacement had a minimum value of 0 mm and a maximum value of 8 mm and was applied as a ramp over 100 equal increments. The displacement range coincided with the range used later during experimental characterization. The interface between each pair of adjacent layers was chosen to be a contact surface with a penalty friction formulation. As with the two-layer jamming structures, a uniform mesh of square elements was used, and each layer had two elements across its thickness.

A mesh refinement study was conducted to ensure that a finer mesh was not required. The study was performed for a twenty-layer jamming structure with vacuum pressure $P = 71.1\ kPa$ and coefficient of friction $\mu = 0.65$. The number of elements across the thickness of each layer was varied between one and four (i.e., the areal density of elements was varied by a factor of sixteen). The one-element simulation did not converge; however, the two-, three-, and four-element simulations converged successfully. In each of the converged simulations, the transverse load and maximum deflection were extracted at each displacement increment. The converged simulations produced force-versus-maximum-deflection curves that were nearly indistinguishable (**Figure S3A**). The mean force difference between the two- and three-element simulations was $0.050\ N$ (0.54% of the range of the two-element simulation), and the mean difference between the two-and four-element simulations was $0.073\ N$ (0.78% of the range of the two-element simulation). Thus, it was deemed sufficiently accurate to mesh each layer with just two elements across its thickness.

The three major design inputs (i.e., the number of layers n, vacuum pressure P, and coefficient of friction μ) were then systematically varied. The quantity n was varied from 5 to 20 in increments of 5 (with $P = 71.1\ kPa$ and $\mu = 0.65$); P was varied from $23.7\ kPa$ to $71.1\ kPa$ in increments of $23.7\ kPa$ (with $n = 20$ and $\mu = 0.65$); and μ was varied from 0.25 to 1 in increments of 0.25 (with $n = 20$ and $P = 71.1\ kPa$). For each set of design inputs, the transverse force and maximum deflection were extracted at each displacement increment. Recall that the effective stiffness k is simply the slope of the force-versus-maximum-deflection curve.

Aside from providing information about the macroscopic deformation of many-layer jamming structures, the finite element models also illustrated the microscopic phenomenon of the slipping of adjacent layers along their interface at high loads (**Figure S3B-C**).

Damping of Many-Layer Jamming Structures

In laminar jamming structures, the layers are coupled via dry friction. The relevant damping phenomenon is Coulomb damping, in which the damping force is independent of the rate of deformation (as opposed to viscous damping, in which the damping force is rate-dependent). Even when jamming structures are loaded quasi-statically, energy is still dissipated. Thus, finite element models of jamming structures subject to static loading are sufficient to characterize damping, and dynamic simulations are not required.

If interfacial velocities (i.e., the velocities at which adjacent layers slip) were high, the damping force could theoretically become rate-dependent. However, from the second

term of equation (33) in **SI: Analytical Modeling: Explicit Solution**, interfacial displacements are observed to scale with $\frac{h}{L}$ times the transverse deflection, where h is the thickness of a layer and L is the length. In the jamming structures analyzed in the paper, h is smaller than L by four orders of magnitude; thus, interfacial velocities are negligible unless transverse velocities are exceptionally high.

The finite element models to analyze damping were built according to the same process as the finite element models to analyze stiffness. However, after the maximum input displacement of $8\ mm$ was applied, the transverse load was reduced to $0\ N$ over 100 equal increments. The force-versus-maximum-deflection curves then illustrated hysteresis, and the area under the curves depicted the energy dissipated over the loading cycle (**Figure S4**).

Recall that the effective damping d is simply the dissipated energy per unit deflection. The quantity d was not explicitly calculated, but can easily be determined. For each point on the force-versus-maximum-deflection curve, an elastic unloading line can be drawn (with a slope equal to that of the pre-slip loading line), and the area under the resulting curve can be computed. This area is the dissipated energy at that particular deflection. After performing this procedure for all points, the dissipated energy can then be plotted against deflection. The value of d is the slope of this curve.

Functional Dependencies

The finite element simulations for the many-layer jamming structures were rerun over an extended displacement range (from $0\ mm$ to $16\ mm$ over 400 equal increments) to ensure that all structures entered the full-slip regime, allowing accurate measurement of full-slip stiffness and damping. Furthermore, the simulations were executed for larger sets of the design inputs to provide more data points for determining functional dependence. The numbers of layers examined were $2, 5, 7, 10, 12, 13, 15, 17, 18,$ and 20; the vacuum pressures were $0.34, 11.9, 23.7, 35.6, 47.4, 59.3, 71.1, 83.0, 94.8,$ and $101.1\ kPa$; and the coefficients of friction were $0.1, 0.2, 0.25, 0.3, 0.4, 0.5, 0.6, 0.7, 0.75,$ and 0.8.

For each simulation, best-fit lines were fit to the first 1% and the last 1% of the force-versus-maximum-deflection curve. The slope of the former line approximated the effective stiffness k during pre-slip, whereas the slope of the latter line approximated k during full-slip. A best-fit line was then fit to the last 1% of the dissipated-energy-versus-maximum-deflection curve. The slope of this line approximated the effective damping d during full-slip. (Recall that d during pre-slip is simply 0).

For each design input (e.g., number of layers), each performance metric (e.g., pre-slip stiffness) was plotted against the values of the design input (e.g., 2 layers, 5 layers, 7 layers, etc.). Based on the formulae derived in the analytical model for two-layer jamming structures, it was hypothesized that the performance metrics for many-layer jamming structures had polynomial dependence on the design inputs. Thus, best-fit polynomials were fit to each plot; however, the appropriate order for each polynomial needed to be determined.

Best-fit polynomials from zero- to fourth-order were tested on each plot, and the root-mean-square error e_{rms} was computed for each polynomial. From physical reasoning,

pre-slip stiffness should be unaffected by the coefficient of friction μ and the vacuum pressure P, as jamming structures are cohesive in pre-slip; thus, the pre-slip stiffness should have zero-order dependence on μ and P. When zero-order polynomials (i.e., flat lines) were fit to the pre-slip stiffness plots for μ and P, it was found that $e_{rms} \cong 0.0070 \frac{N}{mm}$. This value quantified numerical noise in the finite element simulations and was used as the cutoff for determining the appropriate order of the best-fit polynomial for the other stiffness plots. Specifically, for a given pre-slip or full-slip stiffness plot, the lowest-order best-fit polynomial for which $e_{rms} \leq 0.0070 \frac{N}{mm}$ was determined to be the appropriate polynomial.

For the full-slip damping plots, dimensional analysis suggested that the e_{rms} threshold should be multiplied by a characteristic length in order to exhibit the correct units (i.e., $[N]$). As the layers in a jamming structure slip in the direction of their length, the length $L = 250\ mm$ was chosen as the characteristic length, and $e_{rms} \cong 0.0070 \frac{N}{mm} * 250\ mm = 1.8\ N$ was used as the cutoff for determining the appropriate order of the best-fit polynomial for the damping plots.

The polynomial orders were then tabulated to assess functional dependencies (**Table S1**). As expected, pre-slip and full-slip stiffness scaled with $n^3$and n, respectively, where n is the number of layers. Full-slip stiffness also scaled with P and μ^2. In contrast, the analytical model predicted that the full-slip stiffness of a two-layer jamming structure was independent of P and μ. The dependence of full-slip stiffness on these quantities in the finite element model is likely a result of contact pressure distributions arising from the concentrated load and roller supports.

Full-slip damping scaled with n, P, and μ. Damping should scale with the number of interfaces, which in turn scales with n; furthermore, damping should scale with the frictional stress at the interfaces, which again is equal to μP everywhere during full-slip. Thus, these scaling relationships are also physically reasonable. Note that the scaling of full-slip damping with P and μ was also predicted by the analytical model for a two-layer jamming structure.

For practical applications, one final functional dependence is critical: the dependence of the first transition load for a many-layer jamming structure (i.e., the load at which the jamming structure moves from the pre-slip regime to the transition regime) on the design inputs. However, finite element analysis was not necessary to determine this dependence; as described earlier, the first transition load can be accurately predicted by Euler-Bernoulli beam theory and scales with n, P, and μ (**SI: Analytical Modeling: Extending the Model**). Note that the scaling of this load with P and μ was predicted by the analytical model for a two-layer jamming structure as well.

Limiting Behavior

For practical applications, the limiting behavior of jamming structures may be useful to examine. Consider an application in which the bending stiffness ratio between the jammed and unjammed states must be maximized (e.g., for a splint that must gently conform to the shape of a limb and then stiffen to immobilize a joint). This goal can be accomplished by constructing the layers out of exceptionally thin material (e.g., metal foil) and stacking as many layers as possible within the total allowable height H.

When the structure is unjammed, the stiffness will be negligible, as the layers are thin and flexible. When the structure is jammed, the stiffness will be equal to that of a cohesive metal structure of height H.

Nevertheless, such a configuration may have adverse consequences. If the structure is jammed and unintentionally forced into the full-slip regime (e.g., upon a collision), the structure will then exhibit a stiffness approximately equal to its unjammed stiffness; because the unjammed stiffness is negligible, the structure will yield catastrophically if the load is maintained. Obtaining accurate predictions of the load-deformation curve during the transition regime and full-slip may help designers avoid such consequences. Unfortunately, many-layer finite element simulations can be computationally expensive when the number of layers (and in turn, the number of contact interactions) are particularly large.

One solution would be to approximate the system by the limiting case in which the layers of the jamming structure are infinitesimally thin, and an infinite number of layers are stacked within the height H. In other words, the structure is approximated as a continuum. The structure may then be modeled as a single crystal with a single slip system, with slip planes parallel to the xz-plane and the slip direction parallel to the x-axis. The structure may then be computationally modeled using existing finite element packages for crystal plasticity.

Variable Kinematics

The variable kinematics system was modeled as four parts: one rubber substrate and three jamming structures adhered to the bottom. The substrate was approximated as a 2D plane-strain structure with in-plane dimensions of $150\ mm$ x $20\ mm$. Each jamming structure represented a twenty-layer jamming structure, but was approximated as a homogeneous 2D plane-strain structure. The in-plane dimensions of each jamming structure were $49.33\ mm$ x $20\ mm$, and the thickness was equal to the total thickness of twenty layers of paper (i.e., $2\ mm$). Adjacent jamming structures were separated by $1\ mm$ gaps.

Both the substrate and the jamming structures were approximated as elastic. The substrate in subsequent experimental validation was cast from high-stiffness PDMS rubber (Sylgard 184, Dow Corning, Midland, MI). To accurately model this substrate in finite element simulations, the stress-strain curve reported in the literature for the PDMS rubber in uniaxial tension was digitally traced over small deformations.[34] The elastic modulus was determined by computing the slope of the curve, and this elastic modulus (i.e., $19.1\ MPa$) was assigned to the substrate in the finite element model.

Each jamming structure was assigned an elastic modulus in its vacuum-on state and its vacuum-off state. In the vacuum-on state, the elastic modulus equaled that of paper ($6\ GPa$); in the vacuum-off state, the elastic modulus was reduced by a factor of n^2 ($15\ MPa$). The substrate and jamming structures were assigned a Poisson's ratio of 0.49 and 0.156, respectively. Finally, as described in the main text, the thickness of the rubber substrate was chosen such that the bending stiffness of the substrate (k_{sub}) was the geometric mean of the bending stiffness of the jamming structures in the vacuum-off state (k_{jam}^{nv}) and the bending stiffness in the vacuum-on state (k_{jam}^{v}). Because the jamming structures were intended to deform exclusively in the pre-slip

regime, standard Euler-Bernoulli beam theory could be used to approximate bending stiffness simply as EI, where E is the elastic modulus and I is the second area moment of inertia. Using this approximation, the desired thickness of the rubber substrate was 5.0 mm.

One end of the rubber substrate was fixed. To approximate the effect of cable actuation, a pure moment load was applied to a point on the free end. Two simulations were executed: one where the jamming structures were assigned their vacuum-off elastic modulus, and another where they were assigned their vacuum-on modulus. The magnitude of the moment loads were chosen such that the free end of the rubber substrate would nearly contact the fixed end at maximum load; the vacuum-off simulation had a maximum load of $350\ N \cdot mm$, and the vacuum-on simulation had a maximum load of $1\ N \cdot mm$. The loads were applied as ramps over 400 equal increments, and large deformation analysis was enabled. A uniform mesh was used that consisted of square four-node bilinear plane-strain quadrilateral hybrid elements with reduced integration (CPE4RH). Four elements were used across the thickness of the structure.

For both the vacuum-on and vacuum-off cases, the shape of the variable kinematics system was visualized at each load increment. In addition, the coordinates of the nodes along the ventral surface of the system (i.e., the longitudinal surface with the smaller radius of curvature when the system was actuated) were extracted at each load increment. The exact local curvatures were then calculated along the surface using appropriate first and second derivatives of the coordinates.

Experimental Characterization

Fabrication Process

The many-layer jamming structures used in experimental characterization consisted of three parts: strips of copy paper (HP Ultra White Multipurpose Copy Paper), an envelope of thermoplastic polyurethane with a thickness of $0.038\ mm$ (American Polyfilm, Inc., Branford, CT), and thermoplastic polyurethane tubing with an outer diameter of $3\ mm$ (Eldon James Corp., Denver, CO).

The fabrication process for the laminar jamming samples consisted of five major steps (**Figure S4**). First, the strips of copy paper were manufactured. Sheets of copy paper were placed on a laser cutter (VLS4.60, Universal Laser Systems, Inc., Scottsdale, AZ), and strips were cut along the machine direction of the paper (i.e., the long axis) (**Figure S4A**).

Next, the thermoplastic polyurethane (TPU) envelope was created. A frame was cut on the laser cutter from acrylic plastic (**Figure S4B**); this frame defined the region of the TPU sheet that would be sealed in a later step. Since the TPU sheet was intended to form an envelope around the paper strips and TPU tubing, the shape of the frame comprised a close perimeter around these contents. Furthermore, since the frame would be in contact with hot elements in subsequent steps, it was coated with polytetrafluoroethylene (PTFE) tape to prevent adherence.

The TPU sheet was then formed to the acrylic frame on a vacuum former (Formech 300XQ, Formech International Limited, Hertfordshire, United Kingdom) to create a pocket in which to place the paper and tubing (**Figure S4C**). After placing the paper and tubing into the pocket, the sheet of TPU was folded once upon itself to enclose the pocket (**Figure S4D**). The TPU sheet was then covered temporarily with a PTFE sheet and heat-sealed using a one-sided heat press (Powerpress, Fancierstudio, Hayward, CA) at $100\ °C$. Since the heat conduction to the TPU was greatest through the acrylic frame, only the region of the TPU sheet in contact with the frame was sealed, forming an envelope.

To prevent leakage of air into the envelope, another step was performed to improve the bond between the TPU envelope and the TPU tubing. A block of aluminum-6061 was machined with a circular channel through its center, with the diameter of the channel equal to the diameter of the tubing. The block was then sawed in half through the channel, and each half was placed on either side of the tubing, sandwiching the tubing between the two sides of the TPU envelope (**Figure S4E**). The assembly was then covered temporarily with a PTFE sheet and heat-sealed at $171\ °C$. Since only the aluminum blocks were in contact with the heating element of the heat press, only the region of the TPU envelope between the blocks was sealed. Thus, a circumferential seal of the TPU envelope onto the tubing was achieved. The jamming envelope was then trimmed to its final form (**Figure S4F**).

Repeatability Analysis

Five twenty-layer jamming structures were fabricated. Each sample was placed in a universal materials testing device (Instron 5566, Illinois Tool Works, Norwood, MA) and centered on a static three-point bending fixture (Instron 2810-400) with the supporting anvils ($10\ mm$ diameter) set $130\ mm$ apart (**Figure S5A**).

Vacuum pressure was controlled using a manual vacuum regulator (EW-07061-30, Cole-Parmer, Vernon Hills, IL). The TPU tubing in each sample was connected to the regulator via highly flexible polyurethane tubing in order to mitigate parasitic loading of the sample by the rigid regulator. Prior to each test, a vacuum pressure of $68 \pm 1.7\ kPa$ was applied, and a roller was used to remove residual air pockets from the sample.

The loading anvil ($10\ mm$ diameter) was attached to a $100\ N$ load cell (Instron 2525-807) and lowered at a rate of $5\frac{mm}{min}$ until contacting the sample. When the load cell measured a value of $0.010\ N$, the transverse force and displacement of the loading anvil began to be recorded. The anvil was then lowered at a rate of $25\frac{mm}{min}$ until reaching a maximum displacement of $8\ mm$. Tests were conducted at approximately 20% relative humidity. After each test, the sample was disconnected from the regulator and gently flexed multiple times to accelerate its return to ambient pressure. Each sample was tested ten consecutive times.

Occasionally, the loading anvil initially contacted the jamming structure at protruding corners of the seam of its polyurethane envelope; this initial contact caused the materials testing device to undesirably begin measuring force and deflection prior to contacting the bulk of the jamming structure. To discard measurements of the corners of the envelope, we neglected data collected before a small initial force threshold of

$0.050\ N$ was reached, and we defined zero deflection as the deflection at this threshold. This procedure was always implemented, except for cases in which the force range during a test was comparable to $0.050\ N$ (e.g., for five-layer samples in later experimental characterization). No further filtering or smoothing was performed on the raw data.

For each sample, transverse force was plotted against maximum deflection for all ten trials. A mean curve was generated, and standard deviations were computed at each point on the mean curve (**Figure S5B-F**). The maximum standard deviation at any deflection was $0.2516\ N$, which constituted 2.881% of the range of the mean curve for that sample. Thus, the mechanical behavior of the structures was highly repeatable from trial to trial, indicating that fatigue was negligible over the examined range of forces and deflections.

The mean curves of all five samples were then aggregated, and a mean curve of the mean curves was generated (**Figure S5G**). The maximum standard deviation at any deflection was $0.1233\ N$, which constituted 1.414% of the range of the curve. Thus, the mechanical behavior of the structures was also highly repeatable from sample to sample, demonstrating that the fabrication process was sufficiently precise. Together, the high trial-to-trial and sample-to-sample repeatability of the jamming structures showed that many samples and trials were not required in order to collect statistically representative data during experimental characterization.

Materials Testing

To provide a fair comparison between experimental and finite element results for many-layer jamming structures, the elastic modulus E and coefficient of friction μ of the copy paper used in the jamming samples were experimentally measured; these values were then used as material properties of the layers in the finite element simulations. The elastic modulus was measured to be approximately $6\ GPa$, and the coefficient of friction was measured to be approximately 0.65. Both properties were measured according to methods outlined in international paper testing standards,[35,36] and the values fell within the ranges reported in literature.[37,38] The Poisson's ratio of the copy paper was challenging to measure; thus, a literature value of 0.156 was used instead.[37]

Stiffness Characterization Process

The stiffness characterization tests were identical to those conducted for the repeatability analysis (**SI: Experimental Characterization: Repeatability Analysis**). However, fewer samples were tested and fewer trials were executed, as the repeatability analysis showed that many samples and trials were unnecessary. When conducting the tests for the effect of number of layers on stiffness, three samples were fabricated for each number of layers (i.e., three five-layer samples, three ten-layer samples, etc.), and each sample was tested four times at a constant vacuum pressure of $71.1 \pm 1.7\ kPa$. When conducting the tests for the effect of vacuum pressure, three twenty-layer samples were made in total, and each sample was tested four times at vacuum pressures of $0, 23.7 \pm 1.7, 47.4 \pm 1.7$, and $71.1 \pm 1.7\ kPa$. No tests were conducted for the effect of coefficient of friction, as this property could not be precisely varied experimentally.

For each testing group, transverse force was plotted against maximum deflection for all trials. Recall that the effective stiffness k of a jamming structure in three-point bending is equal to the slope of the force-versus-maximum-deflection curve. Again, mean curves were generated, and standard deviations were computed at each point on the mean curve.

Damping Characterization Process

To evaluate finite element predictions for how major design inputs affected the damping of many-layer jamming structures, the damping of jamming structures was experimentally characterized as well. The tests were identical to those conducted for the stiffness characterization. However, after the loading anvil reached its maximum displacement of $8\ mm$, it was then retracted at a rate of $25\ \frac{mm}{min}$ until returning to its original position of $0\ mm$. The transverse force and displacement experienced by the loading anvil continued to be recorded during its retraction. Thus, the behavior of the jamming structures was measured both during loading and unloading.

Due to the extreme similarity of the damping characterization tests to the stiffness characterization tests, a minimal number of samples were tested, and a minimal number of trials were conducted. When conducting the tests for the effect of number of layers on damping, one sample was fabricated for each number of layers, and each sample was tested once at a constant vacuum pressure of $71.1 \pm 1.7 kPa$. When conducting the tests for the effect of vacuum pressure, one twenty-layer sample was made, and the sample was tested once at vacuum pressures of $0, 23.7 \pm 1.7, 47.4 \pm 1.7$, and $71.1 \pm 1.7\ kPa$.

For each test, transverse force was plotted against maximum deflection for all trials. The unloading of the sample during each test allowed the hysteresis curve to be observed. The area under each hysteresis curve depicted the energy dissipated during the loading cycle, and the effective damping d was simply the energy dissipated per unit deflection. Finite element results for many-layer jamming structures accurately predicted experimental results (**Figure S6**). Thus, finite element simulations were not only able to predict the stiffness of many-layer jamming structures, but also their damping behavior.

Functions and Applications

All molds for the subsequent demonstrations were designed using CAD software (SolidWorks 2015, Dassault Systèmes, Villacoublay, France) and 3D printed using a stereolithography-based printer (Objet30 Scholar, Stratasys, Ltd., Eden Prairie, MN).

Shape-Locking

A soft pneumatic bending actuator was designed and fabricated based on previous literature.[2,39] The top of the actuator (i.e., the inflatable chambers) was cast using a two-part mold, whereas the bottom (i.e., a thick, flat layer to promote bending rather than extension) was cast using a one-part mold. All parts were cast from shore 10A platinum-cure silicone rubber (Dragon Skin 10 Medium, Smooth-On, Inc., Macungie, PA). A twenty-layer jamming structure was then designed and fabricated using the

techniques described earlier (**SI: Experimental Characterization: Fabrication Process**). The structure spanned the ventral surface of the actuator (i.e., the longitudinal surface with the smaller radius of curvature when the actuator was pressurized). Finally, the actuator and jamming structure were bonded using silicone building sealant (Dow Corning 795, Dow Corning, Midland, MI).

The actuator and jamming structure were connected to pressure and vacuum inputs, respectively. The pressure source was regulated by a digital pressure regulator (ITV1031, SMC Pneumatics, Yorba Linda, CA), whereas the vacuum source was regulated by the device used in experimental characterization. The output from each of the regulators passed through two miniature pneumatic solenoid valves (V^2 Valves, Parker Hannifin, Hollis, NH) before entering the actuator and jamming structure. The valves were controlled by pushbuttons and enabled the actuator and jamming structure to each have three states: a pressurizing (or vacuuming) state, a hold state where the internal pressure (or vacuum) is preserved, and a depressurizing (or vacuum-relieving) state.

The actuator was pressurized to $16\ kPa$, and a photograph was taken perpendicular to the bending plane. Two tests were then conducted. In the first test, the actuator was depressurized to $0\ kPa$. In the second test, a vacuum of $85\ kPa$ was first applied to the jamming structure, and the actuator was then depressurized to $0\ kPa$. A photograph was again taken once the system came to rest.

For each photograph, the arc of the ventral surface of the shape-locking system was digitally traced. The data points comprising each arc were then interpolated over 100 equally spaced points. The coefficient of determination (R^2) value was computed between the two interpolated arcs.

Variable Kinematics

The substrate of the variable kinematics system was fabricated according to the same process used for the actuator component of the shape-locking system. However, the substrate was cast using a one-part mold with an inserted hexagonal rod, which created a channel to route a cable; furthermore, the substrate was cast from high-stiffness PDMS rubber (Sylgard 184, Dow Corning, Midland, MI). The jamming structure was also designed and fabricated according to the techniques described earlier, but with three distinct stacks of twenty strips separated by $1\ mm$ gaps within the TPU envelope. The jamming structure and rubber substrate were again bonded with silicone building sealant (Dow Corning 795, Dow Corning, Midland, MI).

Braided polyethylene cable (Hollow Spectra, BHP Tackle, Harrington Park, NJ) was then routed through the channel in the substrate. The cable was tied at one end to a turnbuckle and at the other end to a small washer. During testing, the turnbuckles were manually twisted, which pulled the cable, compressed the washer against the end of the variable kinematics structure, and induced bending.

Two-Fingered Grasper

Each fingertip in the two-fingered grasper had a cylindrical surface with a radius of $5\ mm$. The fingertips were cast using a two-part mold according to the same process

used for the shape-locking actuator and variable-kinematics substrate; however, the fingertips were cast from shore 00-10A silicone rubber (Ecoflex 00-10, Smooth-On, Inc., Macungie, PA).

To test bending stiffness and off-axis bending stiffness, the cable was removed from the finger being tested, and the finger was clamped in the vertical position. A digital force gauge (Chatillon DFI10, AMETEK Sensors, Test & Calibration, Berwyn, PA) was moved along a rigid guiderail until contacting the finger $25\ mm$ from its distal end. The force gauge was then pushed forward in $12.5\ mm$ increments. To mitigate viscous effects, approximately five seconds were allowed to elapse, and the force measurement was then recorded. The test was conducted with vacuum off and vacuum on. When measuring bending stiffness, the force gauge was pushed in the direction of the thickness of the substrate; when measuring off-axis bending stiffness, the gauge was in the direction of the width. Because the minimum force measurable by the force gauge was $0.05\ N$, any reading of $0.00\ N$ was rounded to $0.05\ N$; thus, the stiffness increases reported in the main text were worst-case (i.e., lowest possible) estimates.

To measure the torsional stiffness of the fingers in the two-fingered grasper, a custom testing device was designed and fabricated. In the device, a finger was coupled to a pulley with a radius of $16.25\ mm$, which itself was coupled via a cable to a digital force gauge (Chatillon DFI10 AMETEK Sensors, Test & Calibration, Berwyn, PA) (**Figure S7**). Aside from the finger, cable, and force gauge, all components of the device were 3D printed (Objet30 Scholar, Stratasys, Ltd., Eden Prairie, MN). When the force gauge was pulled, the finger was twisted about its longitudinal axis.

The force gauge was retracted in $12.5\ mm$ increments, and force measurements were recorded at each increment. The force measurements were multiplied by the radius of the pulley to calculate torque. Torque was then plotted against pull distance, and the slope was calculated to quantify the torsional stiffness of the finger.

Additional Concepts

Continuously-Variable Stiffness

As first outlined in a previous study,[18] continuously-variable stiffness can be achieved by stacking multiple jamming structures that have independent vacuum inputs (**Figure S8A**). The bending stiffness of the composite structure is determined by the number of jamming structures that have vacuum applied (**Figure S8B**). If the layers are compliant and the number of layers within each jamming structure is small, the bending stiffness of the composite structure can be selected with high resolution.

Many schemes are possible for distributing layers across the jamming structures. One particularly appealing scheme is a binary distribution (i.e., one 2-layer structure, one 4-layer structure, one 8-layer structure, and so on). With such a scheme, a high dynamic range (i.e., the ratio of the stiffness range to the stiffness resolution) can be achieved.

To demonstrate this behavior, a hypothetical case study was conducted (**Figure S8C**). Consider a continuously-variable stiffness structure consisting of thirty layers. Let k be the bending stiffness of a single layer. Consider the following three methods for

distributing the layers across jamming structures: 1) the layers are distributed by binary numbering across four jamming structures (i.e., one two-layer jamming structure, one four-layer, one eight-layer, and one sixteen-layer), 2) the layers are distributed nearly equitably across four jamming structures (i.e., two seven-layer structures and two eight-layer structures), and 3) the layers are distributed equitably across fifteen jamming structures (i.e., fifteen two-layer structures).

The four-structure binary scheme has the superior stiffness range, best-case resolution, and maximum dynamic range, as well as a high number of unique stiffness values; furthermore, with four vacuum inputs, it is simple to physically implement. The fifteen-structure equitable scheme has superior worst-case resolution and minimum dynamic range, as well as the highest number of unique stiffness values; on the other hand, with fifteen inputs, it is challenging to implement. For most applications, a binary scheme may be preferred.

Continuously-Variable Damping

From finite element analysis, it was found that the full-slip damping of a many-layer jamming structure scales linearly with vacuum pressure. Thus, continuously-variable damping can be achieved simply by varying the vacuum pressure on a single jamming structure (**Figure S8D**).

Finite element analysis also showed that the full-slip damping of a many-layer jamming structure scales linearly with the number of layers. In practical applications where high damping is desired but the pressure gradient is limited (e.g., with vacuum, where the gradient is limited to the ambient pressure), the maximum damping value of a continuously-variable damping structure can be augmented in advance by increasing the number of layers in the jamming structure during fabrication (**Figure S8E**). Note that the maximum damping value can also be augmented by increasing the coefficient of friction of the layers.

In other practical applications, damping may be desired over the full range of deformation of the jamming structure. However, as described earlier, damping of a many-layer jamming structure is zero during pre-slip, creating a dead zone for damping; thus, the deformation range over which pre-slip occurs should be minimized. As also described earlier, the pre-slip stiffness of a many-layer jamming structure scales with n^3, whereas the load at which the structure begins to slip (i.e., the maximum load of pre-slip) scales with n (**SI: Finite Element Analysis: Functional Dependencies**). In turn, the deformation at which the structure begins to slip (i.e., the maximum deformation of pre-slip) scales with n^{-2}. Thus, the deformation range over which pre-slip occurs can be minimized in advance by again increasing the number of layers in the jamming structure during fabrication (**Figure S8E**).

In conclusion, continuously-variable damping can be achieved by simply varying the vacuum pressure on a many-layer jamming structure. In practical applications that require high energy dissipation over a maximal range of displacements with a minimal dead zone, such a structure should be fabricated with as many layers as possible.

Spring-Based Jamming

As an alternative to fluidic and electrostatic means for actuating jamming structures, a spring-based actuation method can be implemented (**Figure S9**). In this method, elastic elements (e.g., spring clips) are arranged along the length of a jamming structure that is enclosed in an airtight envelope. In its default state, the elastic elements cause the layers in the jamming structure to be cohesive, and the structure is stiff. However, when the airtight envelope is pressurized, the elastic elements are pushed apart, allowing the layers to slip freely; the jamming structure is compliant and can be reconfigured.

A spring-based actuation method has two distinct advantages. First, the maximum frictional stress at the interfaces between layers can be set to arbitrarily high values by using clips with a higher (or adjustable) spring constant. As described earlier, the load at which a jamming structure begins to slip scales with the pressure gradient P (**SI: Finite Element Modeling: Functional Dependencies**); thus, the structure can maintain its pre-slip stiffness over larger loads than a jamming structure that is actuated by vacuum pressure. Second, the structure only requires power to change its shape, not to preserve it. In applications where the time spent reshaping the jamming structure is much smaller than the time spent locked in a particular configuration, this actuation mechanism can expend negligible energy.

Supplementary Figures

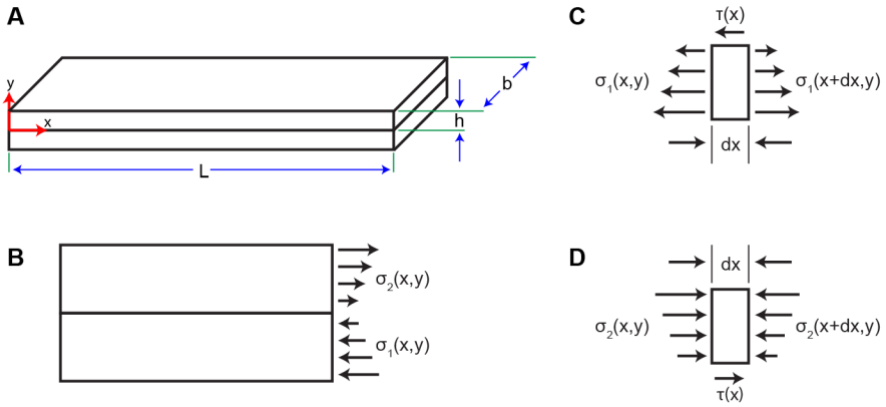

Fig. S1: Diagrams used for analytical derivation of governing equations. *A) The coordinate system and dimensions for the two-layer jamming structure are defined. B) To derive the first governing equation, the resultant moment over the cross-section was computed. The resultant moment is defined as the integral of the moment of stress about the x-axis over the cross-sectional area. One possible stress distribution at a cross-section is shown. C) To derive the second governing equation, static force equilibrium of a thin section of the bottom beam was performed. Stresses were integrated over area to compute force. One possible stress distribution about a thin section is shown. D) To derive the third governing equation, static force equilibrium of a thin section of the top beam was performed.*

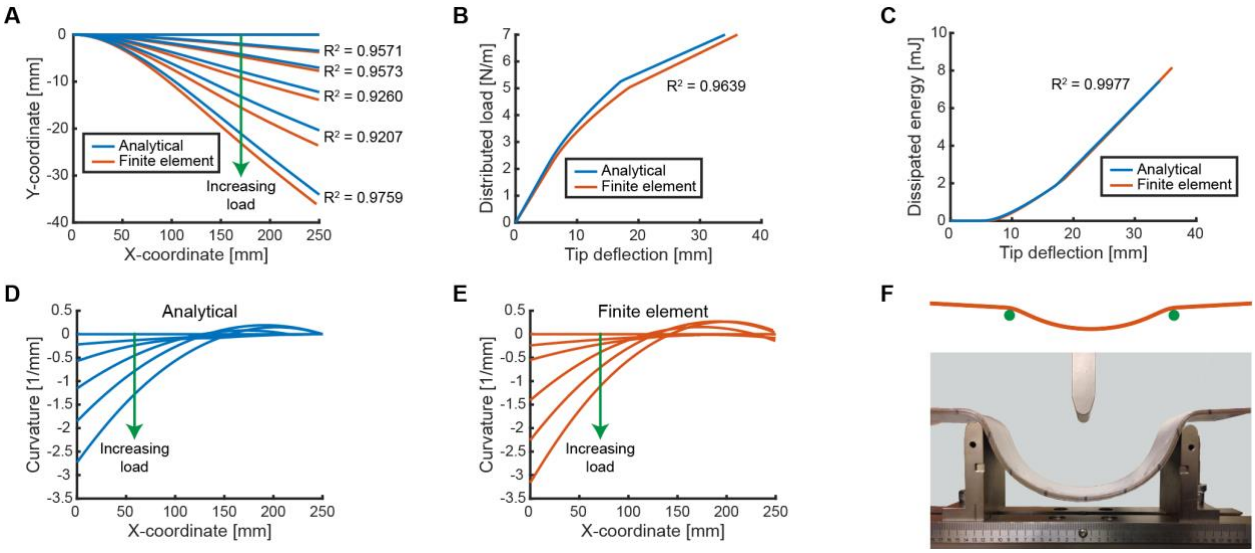

Fig. S2: Finite element evaluation of analytical model. *Analytical and finite element models were constructed of a two-layer jamming structure in cantilever bending subject to a uniform distributed load. The models had identical dimensions, material properties, boundary conditions, and loads. The analytical model predicted finite element results with high accuracy in all cases. A) Elastica are compared for six equal load increments from zero load to the maximum load. B) Load-versus-deflection curves are compared. Recall that the effective stiffness k is equal to the slope. C) Dissipated-energy-versus-deflection curves are compared. Recall that the effective damping b is equal to the slope. D) Curvatures are shown for the elastica of the two-layer analytical model. Note that the curvature crosses zero (i.e., reverses sign) for moderate loads and above. E) Curvatures are shown for the two-layer finite element model. The curvature profiles are predicted closely by the analytical model. F) Curvature reversal was also observed for finite element models (Top) and experimental samples (Bottom) of many-layer jamming structures in three-point bending. Sharp curvature reversal can be seen near the supports.*

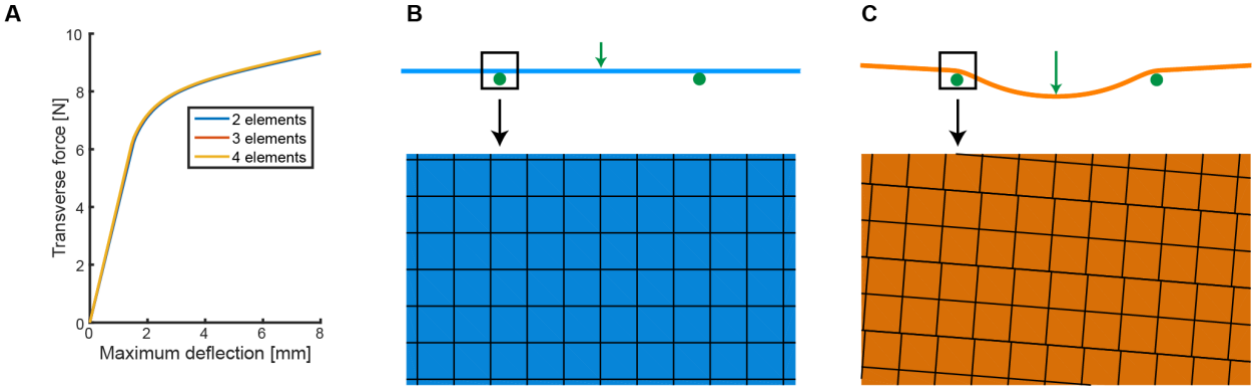

Fig. S3: Finite element mesh refinement study and slip visualization. *A) A mesh refinement study was performed for a twenty-layer finite model in three-point bending. A uniform mesh of square elements was used, and the number of elements across the thickness of each layer was varied between two and four. The resulting force-versus-deflection curves were nearly indistinguishable; thus, two elements across the thickness was sufficiently accurate. B) The many-layer finite element models could illustrate slip between adjacent layers. Slip for a typical twenty-layer model in three-point bending is shown here. During the pre-slip regime, nodes along adjacent interfaces were coincident. C) During the full-slip regime, nodes that were initially coincident moved relative to each other.*

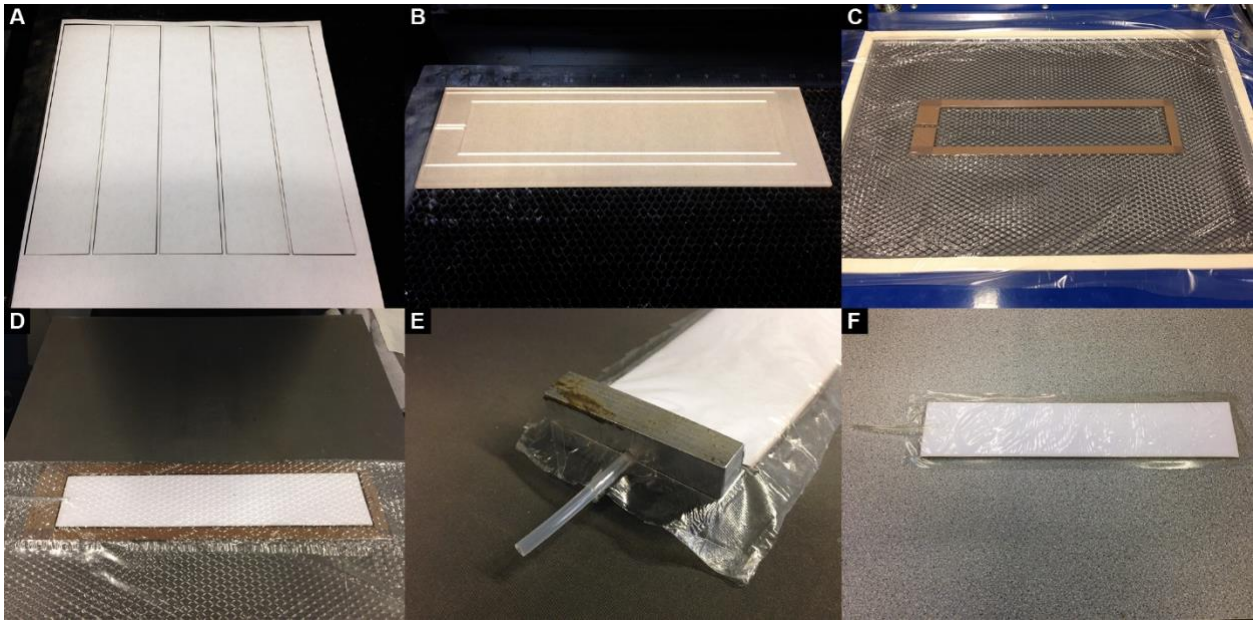

Fig. S4: Fabrication process for real-world jamming structures. *The fabrication process is illustrated for a typical sample of a many-layer jamming structure. A) A sheet of copy paper was placed on the bed of a laser cutter, and strips were cut along the machine direction. B) Acrylic was placed on the bed of the laser cutter, and a frame was cut. C) The frame was coated in PTFE tape and positioned on the bed of a vacuum former. A thin sheet of TPU was formed to the frame. D) The frame and TPU sheet were positioned on the bed of a heat press. The strips of paper and a segment of TPU tubing were placed inside, and the TPU sheet was folded to cover the contents. E) Aluminum blocks with a circular channel were arranged on the top and bottom of the end of the jamming structure, sandwiching the TPU tubing between the two sides of the TPU envelope. F) Fabrication of the sample was completed.*

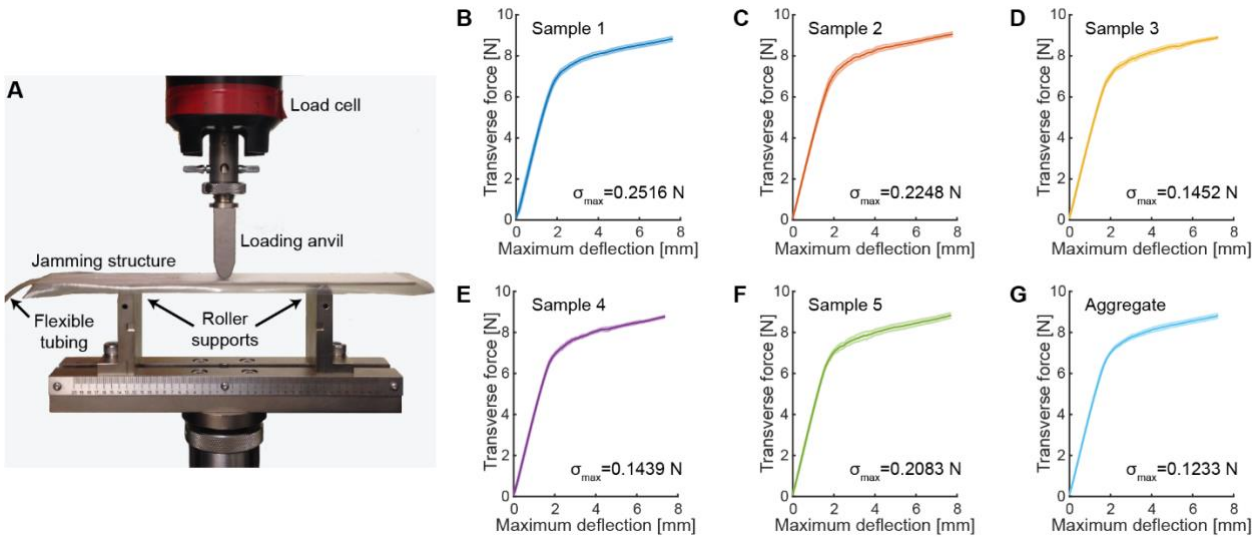

Fig. S5: Testing setup and repeatability analysis for experimental characterization of jamming structures. *A) The jamming structure was placed in a test fixture for three-point bending, which consisted of a loading anvil and two roller supports. The loading anvil was attached to a load cell, and the jamming structure was connected to a vacuum regulator via flexible tubing to mitigate parasitic loading of the tubing on the sample. B-F) Testing results for five twenty-layer jamming structures are shown in sequence. For each sample, a mean curve is plotted, along with a shaded error bar that spans ± 1 standard deviation from the mean. The maximum standard deviation at any deflection is given. The structures were highly repeatable from trial to trial. G) The mean curves for all five samples were then aggregated. A mean curve of the mean curves is plotted, along with a shaded error bar. The structures were highly repeatable from sample to sample.*

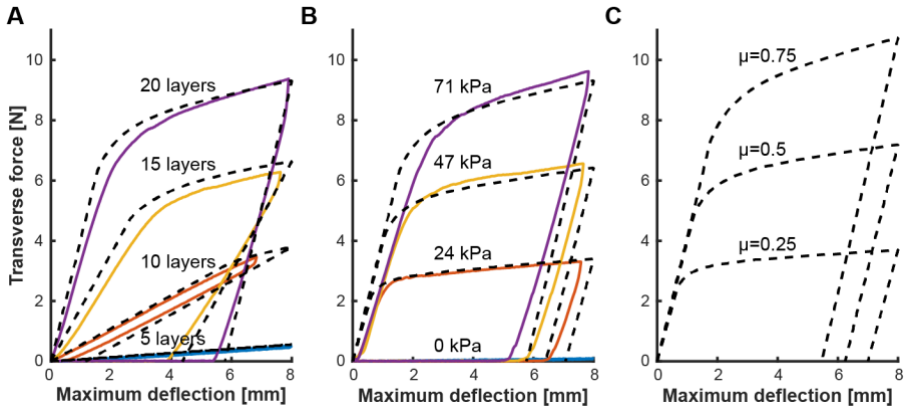

Fig. S6: Finite element predictions and experimental characterization of damping in many-layer jamming structures. *Jamming structures were loaded in three-point bending and subsequently unloaded. Transverse force is plotted against maximum deflection; dashed lines indicate finite element predictions, and colored lines denote experimental results. Finite element models accurately predicted experimentally observed hysteresis. The area under the hysteresis curves is equal to the energy dissipated over the loading cycle, and the effective damping d is equal to the energy dissipated per unit deflection. A) The number of layers in the jamming structures was varied. B) Vacuum pressure was varied. No finite element data is provided for the $0\ kPa$ case, as the model was unstable. C) Coefficient of friction was varied. No experimental data is shown, as coefficients of friction could not be precisely varied experimentally.*

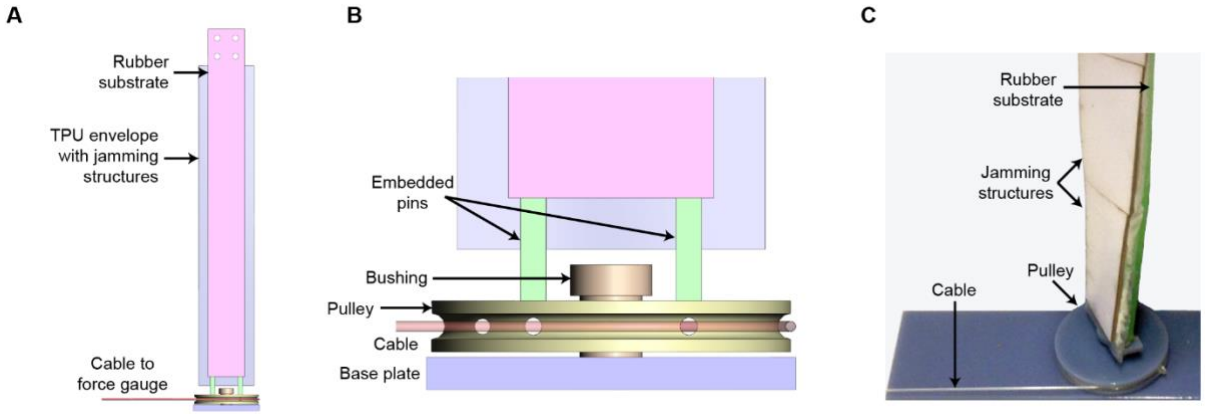

Fig. S7: Testing device for measuring the torsional stiffness of a variable kinematics system*. A) Front view of the testing device. A variable kinematics structure is hung vertically. Its upper end is bolted in place, and its lower end is coupled to a cable that is connected to a force gauge. B) Zoom view of the lower end of the testing device. Two plastic pins are embedded in the variable kinematics structure and fastened to a pulley, and the cable is wound around the pulley. When the cable is pulled, the pulley spins around a bushing, and the variable kinematics structure is twisted about its longitudinal axis. C) Physical implementation of the testing device. The variable kinematics structure was originally oriented as shown in A and B; its lower end has now been twisted by approximately* 80°.

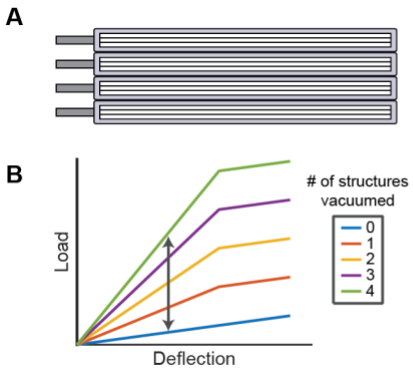

C

	Four-structure binary scheme	Four-structure near-equitable scheme	Fifteen-structure equitable scheme
Number of unique stiffness values	16	9	17
Range	$4650k$	$1680k$	$90k$
Best-case resolution	$6k$	$168k$	$6k$
Worst-case resolution	$3510k$	$336k$	$6k$
Maximum dynamic range	775	10	15
Minimum dynamic range	1.3	5	15

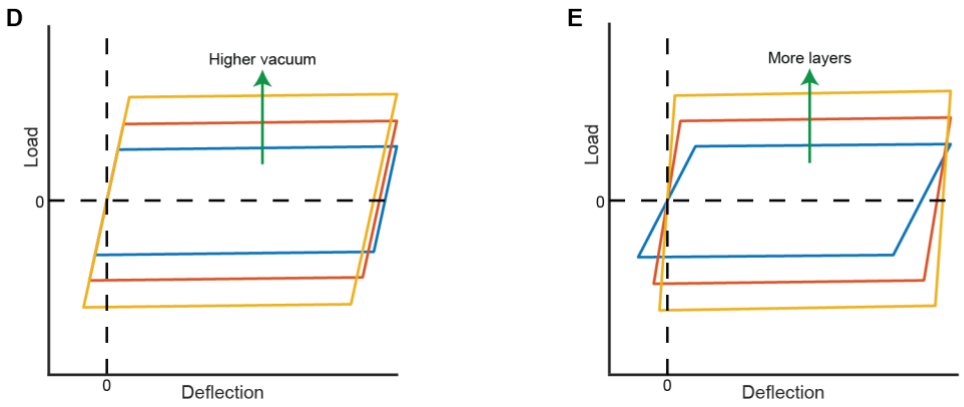

Fig. S8: Conceptual examples of continuously-variable stiffness and damping structures. *For simplicity, transition regimes between the pre-slip regime and the full-slip regime are not depicted. A) In one implementation of continuously-variable stiffness, four jamming structures are stacked and bonded. Each jamming structure has an independent vacuum input and contains three layers of compliant material. B) By applying or relieving vacuum from individual jamming structures, the pre-slip bending stiffness of the composite structure may be selected from one of five possible values. C) For a continuously-variable stiffness structure consisting of thirty total layers, three different ways are considered for distributing the layers across multiple jamming structures. Quantity k is the bending stiffness of a single layer. A four-structure binary scheme is preferable over equitable and near-equitable schemes, as it has the best stiffness range, resolution, and dynamic range, and it is simple to physically implement. D) Conceptual load-versus-deflection curves are shown for a continuously-variable damping structure. (Because it may be desirable to use such a structure over multiple cycles, a full hysteresis loop is shown; the structure is loaded, unloaded, and then loaded and unloaded in the opposite direction to return to zero deflection.) Increasing the vacuum pressure augments the dissipated energy (i.e., the area enclosed by the hysteresis loop) and damping (i.e., the dissipated energy per unit deflection). E) Increasing the number of layers again augments damping. Furthermore, it minimizes the range of deformation over which the pre-slip regime occurs, maximizing the range over which damping is nonzero.*

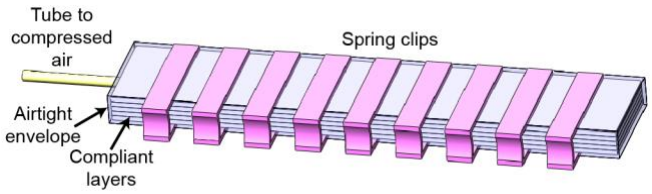

Fig. S9: Conceptual example of a spring-based jamming structure. *A many-layer jamming structure enclosed in an airtight envelope is connected to a compressed air source and has spring clips arranged along its length. When no air is supplied, the spring clips cause the layers to be cohesive, and the structure is stiff. When air is supplied, the clips are pushed open, and the layers can slip freely. The structure is then compliant and may be reconfigured.*

Supplementary Tables

Table S1: Functional dependence of performance metrics on design inputs for many-layer jamming structures. *Regression analysis was used to determine the functional dependence of stiffness and damping on the number of layers,*

vacuum pressure, and coefficient of friction. The relationships between the parameters were well-described by best-fit polynomial functions of the specified order. Root-mean-square (RMS) error is provided for each polynomial relationship.

	Pre-slip stiffness		Full-slip stiffness		Full-slip damping	
	Polynomial order	RMS error $\left[\frac{N}{mm}\right]$	Polynomial order	RMS error $\left[\frac{N}{mm}\right]$	Polynomial order	RMS error $[N]$
Number of layers (n)	3	0.0001	1	0.0006	1	0.0238
Vacuum pressure (P)	0	0.0065	1	0.0028	1	0.1326
Coefficient of friction (μ)	0	0.0072	2	0.0020	1	0.0788

Supplementary Videos

Video S1: Demonstration of real-world jamming structures. A twenty-layer jamming structure was fabricated, and 85 kPa of vacuum pressure was selectively applied. Three distinct functions are demonstrated: tunable stiffness, in which it can change its bending stiffness by several orders of magnitude; shape-locking, in which it can preserve an arbitrary shape; and structural plasticity, in which it can be plasticly formed to arbitrary objects in its vacuumed state due to energy dissipation during the full-slip regime. (Note that the shape-locking function is intended to be used with an actuated soft structure, as in **Figure 4E-F**. Also note that in the structural plasticity demonstrations, strong curvature reversal is exhibited at the boundaries of the plastically deformed regions. See **SI: Analytical Modeling: Curvature Reversal** for more details.)

Video S2: Finite element model of variable kinematics system. A finite element model of a variable kinematics system is subject to an increasing moment load with and without vacuum. With vacuum off, the system displays continuous deformation with nearly constant curvature. With vacuum on, the system exhibits discrete deformation with joints; rigid sections with low curvature are connected by compliant sections with much higher curvature, approximating the kinematics of a traditional articulated manipulator. The discreteness (i.e., the ratio of peak curvature to mean curvature) becomes increasingly pronounced at higher loads.